Magnetotelluric responses of three-dimensional bodies in layered earths

Philip E. Wannamaker*, Gerald W. Hohmann‡, and Stanley H. Ward*

ABSTRACT

The electromagnetic fields scattered by a three-dimensional (3-D) inhomogeneity in the earth are affected strongly by boundary charges. Boundary charges cause normalized electric field magnitudes, and thus tensor magnetotelluric (MT) apparent resistivities, to remain anomalous as frequency approaches zero. However, these E-field distortions below certain frequencies are essentially in-phase with the incident electric field. Moreover, normalized secondary magnetic field amplitudes over a body ultimately decline in proportion to the plane-wave impedance of the layered host. It follows that tipper element magnitudes and all MT function phases become minimally affected at low frequencies by an inhomogeneity.

Resistivity structure in nature is a collection of inhomogeneities of various scales, and the small structures in this collection can have MT responses as strong locally as those of the large structures. Hence, any telluric distortion in overlying small-scale extraneous structure can be superimposed to arbitrarily low frequencies upon the apparent resistivities of buried targets. On the other hand, the MT responses of small and large bodies have frequency dependencies that are separated approximately as the square of the geometric scale factor distinguishing the different bodies. Therefore, tipper ele-

ment magnitudes as well as the phases of all MT functions due to small-scale extraneous structure will be limited to high frequencies, so that one may "see through" such structure with these functions to target responses occurring at lower frequencies.

About a 3-D conductive body near the surface, interpretation using 1-D or 2-D TE modeling routines of the apparent resistivity and impedance phase identified as transverse electric (TE) can imply false low resistivities at depth. This is because these routines do not account for the effects of boundary charges. Furthermore, 3-D bodies in typical layered hosts, with layer resistivities that increase with depth in the upper several kilometers, are even less amenable to 2-D TE interpretation than are similar 3-D bodies in uniform half-spaces. However, centrally located profiles across geometrically regular, elongate 3-D prisms may be modeled accurately with a 2-D transverse magnetic (TM) algorithm, which implicitly includes boundary charges in its formulation. In defining apparent resistivity and impedance phase for TM modeling of such bodies, we recommend a fixed coordinate system derived using tipper-strike, calculated at the frequency for which tipper magnitude due to the inhomogeneity of interest is large relative to that due to any nearby extraneous structure.

INTRODUCTION

Magnetotelluric (MT) measurements are sensitive to the resistivity structure of the earth, potentially to depths exceeding 100 km (Cagniard, 1953; Swift, 1967; Word et al., 1971; Vozoff, 1972; Larsen, 1981; Wannamaker, 1983). Recent advances in instrumentation and data processing (e.g., Gamble et al., 1979; Weinstock and Overton, 1981; Stodt, 1983) have enabled procurement of precise tensor MT data. However, the skills neces-

sary to translate these measurements into trustworthy models of subsurface resistivity have been slow in developing.

MT data are, strictly speaking, responses from three-dimensional (3-D) resistivity structure in the earth, but traditionally they have been interpreted using 1-D and sometimes 2-D model structures (for example, Petrick et al., 1977; Stanley et al., 1977; Rooney and Hutton, 1977). This tradition has arisen because 3-D modeling routines require considerable computing resources to handle complex earth structure, re-

sources not readily available. This shortcoming produces a lack of concensus on the interpretive errors which occur when 1-D and 2-D computational aids are used in 3-D areas.

We favor keeping the interpretation of observations as simple as possible. This philosophy underlies the major purposes of this paper, which are as follows: first, develop magnetotelluric theory for 3-D bodies buried in otherwise 1-D media to establish the fundamental controls on observed responses; and second, investigate the utility of 1-D and 2-D algorithms for interpreting 3-D geology. The latter goal is achievable only through rigorous, three-dimensional model studies, which we perform using the computer program of Wannamaker et al. (1984).

MAGNETOTELLURIC THEORY FOR THREE-DIMENSIONAL BODIES IN LAYERED EARTHS

Here we pursue the essentials that determine the magnetotelluric signatures of three-dimensional bodies. Special attention is paid to understanding the low-frequency limits of MT responses. By incorporating this understanding with standard EM scaling concepts, in our model study we can propose means of discriminating the response of a large resistivity anomaly, which may represent an exploration target, from that of a small one, which may constitute mere extraneous, overlying structure.

Electromagnetic field relations

A 3-D body in the earth is a source of scattered electric and magnetic fields. Establishing relations between the incident plane-wave fields and the scattered and total fields, as well as exploring the behavior of these relations as frequency varies, is an important step toward resolving the roles of the inhomogeneity and the host layering in creating anomalous MT response functions.

Governing equations.—Source-free versions of Maxwell's equations (Harrington, 1961) describe the total, plane-wave induced electric and magnetic fields $(\mathbf{E}, \mathbf{H})$ as a function of position $\mathbf{r}$ about a 3-D body in a layered medium (Figure 1). In the manner of Wannamaker et al. (1984), $(\mathbf{E}, \mathbf{H})$ can be decomposed into an incident set $(\mathbf{E}_i, \mathbf{H}_i)$ which are the plane-wave fields and a secondary set $(\mathbf{E}_s, \mathbf{H}_s)$ contributed by the inhomogeneity. The secondary fields are specified in terms of a scattering current $\mathbf{J}_s = (\hat{y}_b - \hat{y}_j)\mathbf{E}_b$, where $\hat{y}_b$ and $\hat{y}_j$ are the admittivities of the body and of layer j containing the body, while $\mathbf{E}_b$ is the total electric field within the body. If the scattering current within the inhomogeneity is known, the secondary EM fields elsewhere can be given by integral equations (Wannamaker et al., 1984).

Equation (7) of Wannamaker et al. (1984) describes the source of the secondary electric field with a volume current component $\hat{z}\mathbf{J}_s$, where $\hat{z}$ is taken to be the impedivity of free space, and a free-charge component

$$\frac{-1}{\hat{y}_j} \nabla \cdot \mathbf{J}_s.$$

The free charge preserves continuity of normal total current density, but in doing so makes the normal total electric field discontinuous (Price, 1973). Furthermore, since $\mathbf{E}_i$ is continuous, $\nabla \cdot \mathbf{E}_s = \nabla \cdot \mathbf{E}$.
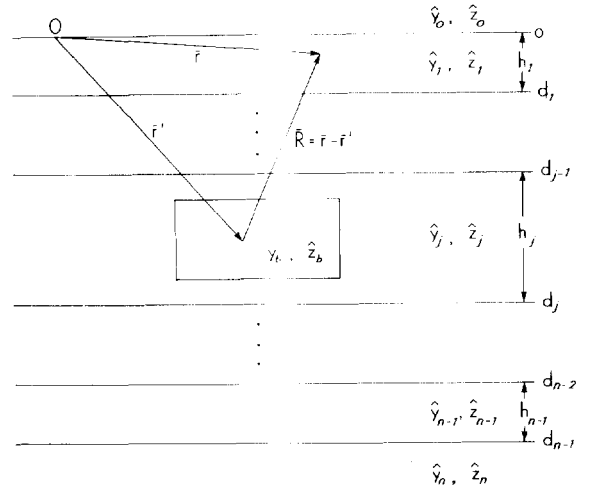
FIG. 1. Section view showing physical properties of a 3-D body in a layered earth.

Tensor field relations.—Considering the linearity of the governing equations of Wannamaker et al. (1984), we postulate

$$\mathbf{E}^0(\mathbf{r}) = \mathbf{E}_i^0 + [\tilde{\mathbf{P}}_s^0(\mathbf{r})] \cdot \mathbf{E}_i^0 \tag{1}$$

and

$$\mathbf{H}^0(\mathbf{r}) = \mathbf{H}_i^0 + [\tilde{\mathbf{Q}}_s^0(\mathbf{r})] \cdot \mathbf{E}_i^0, \tag{2}$$

where superscript zero indicates we are considering $\mathbf{r}$ at the surface of the earth over which $\mathbf{E}_i^0$ is constant. $[\tilde{\mathbf{P}}_s^0(\mathbf{r})]$ and $[\tilde{\mathbf{Q}}_s^0(\mathbf{r})]$ are 3×2 normalized tensors representing the scattered field unique for a specified 3-D body, layered host and frequency, of the form

$$[\tilde{\mathbf{P}}_s^0(\mathbf{r})] = \begin{bmatrix} [\tilde{\mathbf{P}}_{hs}^0(\mathbf{r})] \\ ----- \\ [\tilde{\mathbf{P}}_{vs}^0(\mathbf{r})] \end{bmatrix} = \begin{bmatrix} P_{xx}^0 & P_{xy}^0 \\ P_{yx}^0 & P_{yy}^0 \\ ---- & ---- \\ P_{zx}^0 & P_{zy}^0 \end{bmatrix}, \tag{3}$$

and

$$[\tilde{\mathbf{Q}}_s^0(\mathbf{r})] = \begin{bmatrix} [\tilde{\mathbf{Q}}_{hs}^0(\mathbf{r})] \\ ----- \\ [\tilde{\mathbf{Q}}_{vs}^0(\mathbf{r})] \end{bmatrix} = \begin{bmatrix} Q_{xx}^0 & Q_{xy}^0 \\ Q_{yx}^0 & Q_{yy}^0 \\ ---- & ---- \\ Q_{zx}^0 & Q_{zy}^0 \end{bmatrix}. \tag{4}$$

Note that we have subdivided the scattered field tensors into horizontal subtensors, $[\tilde{\mathbf{P}}_{hs}^0(\mathbf{r})]$ and $[\tilde{\mathbf{Q}}_{hs}^0(\mathbf{r})]$, and vertical subtensors, $[\tilde{\mathbf{P}}_{vs}^0(\mathbf{r})]$ and $[\tilde{\mathbf{Q}}_{vs}^0(\mathbf{r})]$, which pertain, respectively, to horizontal and vertical electric and magnetic field components induced by the incident electric vector $\mathbf{E}_i^0$. Discrete, approximate versions of $[\tilde{\mathbf{P}}_s^0(\mathbf{r})]$ and $[\tilde{\mathbf{Q}}_s^0(\mathbf{r})]$ are computed by Wannamaker et al. (1984). Hermance and Thayer (1975), Larsen (1975, 1977, 1981), Klein and Larsen (1978), Stodt et al. (1981), and Hermance (1982) also considered E- and H-field tensor approaches.

The incident fields at the surface are related through

$$E_i^0 = [\tilde{Z}_\ell] \cdot H_i^0, \tag{5}$$

(Cagniard, 1953; Ward, 1967, p. 117–124), with the layered earth impedance

$$[\tilde{Z}_\ell] = \begin{bmatrix} 0 & Z_\ell \\ -Z_\ell & 0 \end{bmatrix}. \tag{6}$$

Using equations (1) through (5), and with $[\tilde{I}]$ the 2×2 identity tensor, the horizontal fields become

$$E_h^0(\mathbf{r}) = \{[\tilde{I}] + [\tilde{P}_{hs}^0(\mathbf{r})]\} \cdot E_i^0, \tag{7}$$

and

$$H_h^0(\mathbf{r}) = \{[\tilde{I}] + [\tilde{Q}_{hs}^0(\mathbf{r})] \cdot [\tilde{Z}_\ell]\} \cdot H_i^0. \tag{8}$$

Low-frequency conditions.—At low frequencies, such that wavelengths in the host layers are long compared to the observation distance **R** from the body (Figure 1), the Helmholtz equations of Wannamaker et al. (1984) asymptote to Laplace's and Poisson's equations. In particular, note that the volume current source term $\tilde{z}\mathbf{J}_s$ in equation (7) of Wannamaker et al. (1984) vanishes. This term, to first order, is proportional to frequency so that $E_s^0(\mathbf{r})$ and thus $[\tilde{P}_s^0(\mathbf{r})]$ at low frequencies are determined solely by the free charge. However, equation (7) of Wannamaker et al. (1984) shows that the charge density is intimately associated with the E-field inside the inhomogeneity. Also, the E-field interior to the body defines $\mathbf{J}_s$, which in turn provides the source for the secondary magnetic field (op. cit.). We thus require frequencies sufficiently low so that wavelengths within the inhomogeneity are long compared to the size of the inhomogeneity before it is strictly valid to treat the secondary EM fields as though induced by a zero-frequency incident electric field. When both exterior and interior long-wavelength criteria are satisfied, then $[\tilde{P}_s^0(\mathbf{r})]$ and $[\tilde{Q}_s^0(\mathbf{r})]$ will be essentially real and independent of frequency.

In conclusion, with free charges $E^0(\mathbf{r})$ near a 3-D body remains anomalous to arbitrarily low frequencies. Such anomalous behavior due to this charge, when it occurs about conductive bodies, is referred to as current gathering by various investigators (e.g., Berdichevskiy and Dmitriev, 1976). Boundary charges, however, do not enter into $H^0(\mathbf{r})$ as frequency falls. Over an arbitrarily layered earth, it is not difficult to show that $|Z_\ell|$ decreases monotonically with decreasing frequency (see Cagniard, 1953). In particular, for a uniform half-space, we have

$$|Z_\ell| = \left| \frac{\omega\mu_0}{k_1} \right| \simeq \left| \frac{\omega\mu_0}{\sigma_1} \right|^{1/2}, \tag{9}$$

indicating that $[\tilde{Z}_\ell]$ in this case varies as $\omega^{1/2}$ (ω is angular frequency). Hence, even though $[\tilde{Q}_s^0(\mathbf{r})]$ possesses a nonzero, low-frequency limit, $H_s^0(\mathbf{r}) = [\tilde{Q}_s^0(\mathbf{r})] \cdot [\tilde{Z}_\ell] \cdot H_i^0$ will vanish as frequency approaches zero.

Tensor magnetotelluric quantities

The tensor field relations we have specified may be used to construct MT functions. In doing so, the relative contributions of the body and the layered host to anomalous MT functions become evident. Studies of MT functions over single bodies, and in particular the low-frequency asymptotes of such quantities, are required before considering multiple bodies.

Impedance tensor.—The impedance tensor $[\tilde{Z}(\mathbf{r})]$, defined by

$$E_h^0(\mathbf{r}) = [\tilde{Z}(\mathbf{r})] \cdot H_h^0(\mathbf{r}), \tag{10}$$

where $[\tilde{Z}(\mathbf{r})]$ is of the form

$$[\tilde{Z}(\mathbf{r})] = \begin{bmatrix} Z_{xx} & Z_{xy} \\ Z_{yx} & Z_{yy} \end{bmatrix}, \tag{11}$$

can be formulated by substituting equations (7) and (8) into equations (5). One obtains

$$[\tilde{Z}(\mathbf{r})] = \{[\tilde{I}] + [\tilde{P}_{hs}^0(\mathbf{r})]\} \cdot [\tilde{Z}_\ell] \cdot \{[\tilde{I}] + [\tilde{Q}_{hs}^0(\mathbf{r})] \cdot [\tilde{Z}_\ell]\}^{-1}. \tag{12}$$

As frequency approaches zero, equation (12) reduces to

$$[\tilde{Z}(\mathbf{r})] \simeq \{[\tilde{I}] + [\tilde{P}_{hs}^0(\mathbf{r})]\} \cdot [\tilde{Z}_\ell]. \tag{13}$$

All four elements Z_{ij} of $[\tilde{Z}(\mathbf{r})]$ are related to Z_ℓ by real constants, so that in this low-frequency limit a Hilbert transform relates magnitude and phase of Z_{ij} (Kunetz, 1972; Boehl et al., 1977). Also, it is easy to show from equation (13) that the impedance ellipticity (Word et al., 1971) approaches zero as frequency becomes low (and see Ting and Hohmann, 1981).

The apparent resistivities at low frequencies are, from equation (13),

$$\rho_{xx} \simeq \frac{1}{\omega\mu_0} |Z_\ell|^2 \cdot |P_{xy}^0|^2, \tag{14a}$$

$$\rho_{xy} \simeq \frac{1}{\omega\mu_0} |Z_\ell|^2 \cdot |1 + P_{xx}^0|^2, \tag{14b}$$

$$\rho_{yx} \simeq \frac{1}{\omega\mu_0} |Z_\ell|^2 \cdot |1 + P_{yy}^0|^2, \tag{14c}$$

and

$$\rho_{yy} \simeq \frac{1}{\omega\mu_0} |Z_\ell|^2 \cdot |P_{yx}^0|^2 \tag{14d}$$

for a 3-D body. Like the Z_{ij}, all ρ_{ij} are distorted to arbitrarily low frequencies by boundary charge effects and are related to $\rho_\ell = 1/\omega\mu_0|Z_\ell|^2$ by positive constants as given in equation (14). If interpreted assuming a 1-D model structure, apparent resistivity soundings distorted in this manner by a nearby 3-D body will yield model resistivities in error by a factor ρ_{ij}/ρ_ℓ and model layer thicknesses in error by $\sqrt{\rho_{ij}/\rho_\ell}$ (Larsen, 1977, 1981).

However, since the P_{ij}^0 become real as frequency approaches zero, the phases of all Z_{ij} (i.e., ϕ_{ij}) asymptote to the phase of the layered host impedance ϕ_ℓ and are no longer affected by the inhomogeneity. Nevertheless, this does not mean that the parameters of the layered host can be recovered through 1-D inversion of the impedance phase sounding alone. It is well-known in the literature (for example, Cagniard, 1953), and can be inferred from equations (13) and (14), that a specific impedance phase sounding can correspond to an infinite number of apparent resistivity soundings, and thus an infinite number of layered resistivity structures.

Let us now briefly consider a 2-D inhomogeneity, whose strike direction corresponds to the x coordinate axis. An x-oriented incident electric field induces only x-oriented secondary E-fields about such a structure, so that the total electric field parallels all resistivity contacts and no boundary charges exist. This is the transverse electric (TE) mode of wave polarization (Swift, 1967). At low frequencies for the TE mode, neither

volume currents nor boundary charges pertain as sources for a secondary electric field; therefore, P_{xx}^0 becomes zero and ρ_{xy} in equation (14b) approaches ρ_t.

Thus, if all near-surface extraneous structure were 2-D, then 1-D inversion of apparent resistivity and impedance phase soundings identified as TE would yield models of any deep resistivity layering below that are relatively free from distortion due to such structure (Word et al., 1971; Vozoff, 1972; Berdichevskiy and Dmitriev, 1976). On the other hand, if resistivity structures possess finite strike lengths as do the models we will compute, then 1-D inversions in such instances potentially may suffer serious error.

Similarly, a y-oriented incident electric field causes only y-oriented secondary E-fields over a 2-D body. Such a field polarizaton defines the transverse magnetic (TM) mode. However, since the incident electric field for this mode is normal to resistivity contacts in the earth, boundary charges will be induced as sources for secondary E-fields, P_{yy}^0 will have a nonzero value to arbitrarily low frequencies and ρ_{yx} remains defined by equation (14c). Because of boundary charges, the TM mode in the case of conductive bodies exhibits vertical current-gathering (Park et al., 1983).

Tipper transfer tensor.—The tipper transfer function is defined by

$$[\mathbf{H}_z^0(\mathbf{r})] = [\tilde{\mathbf{K}}_z(\mathbf{r})] \cdot \mathbf{H}_h^0(\mathbf{r}), \tag{15}$$

(Word et al., 1970), in which

$$\tilde{\mathbf{K}}_z(\mathbf{r}) = [K_{zx} \quad K_{zy}]. \tag{16}$$

In terms of scattered field tensors, we have

$$[\tilde{\mathbf{K}}_z(\mathbf{r})] = [\tilde{\mathbf{Q}}_{vs}^0(\mathbf{r})] \cdot [\tilde{\mathbf{Z}}_t] \cdot \{[\tilde{\mathbf{I}}] + [\tilde{\mathbf{Q}}_{hs}^0(\mathbf{r})] \cdot [\tilde{\mathbf{Z}}_t]\}^{-1}. \tag{17}$$

The low-frequency asymptotes of the tipper elements are

$$K_{zx} \simeq -Z_t Q_{zy}^0 \tag{18a}$$

and

$$K_{zy} \simeq Z_t Q_{zx}^0. \tag{18b}$$

Note that K_{zx} and K_{zy} are related to Z_t by real constants, so their magnitudes approach zero as frequency approaches zero (Word et al., 1970). In addition, phases of K_{zx} and K_{zy} approach ϕ_t as frequency falls, since $[\tilde{\mathbf{Q}}_{vs}^0(\mathbf{r})]$ becomes real.

The tipper (Vozoff, 1972) has a magnitude given by

$$|T| = [|K_{zx}|^2 + |K_{zy}|^2]^{1/2}. \tag{19}$$

From equation (18), at low frequencies, the tipper likewise becomes zero as $\omega \to 0$. Because of Z_t, T and $[\tilde{\mathbf{K}}_z(\mathbf{r})]$ contain a good deal of information about the layered host.

THREE-DIMENSIONAL MAGNETOTELLURIC MODEL STUDY

The foregoing theoretical concepts are now exemplified using two specific resistivity inhomogeneities. The first is a small-scale, shallow, conductive body. This might represent a single zone of the hydrothermal alteration which is common at geothermal resource areas of the western United States (e.g., Sandberg and Hohmann, 1982) or some other near-surface heterogeneity (SEG Workshop on Magnetotellurics, Las Vegas, 1983). Such heterogeneity can reside directly over exploration
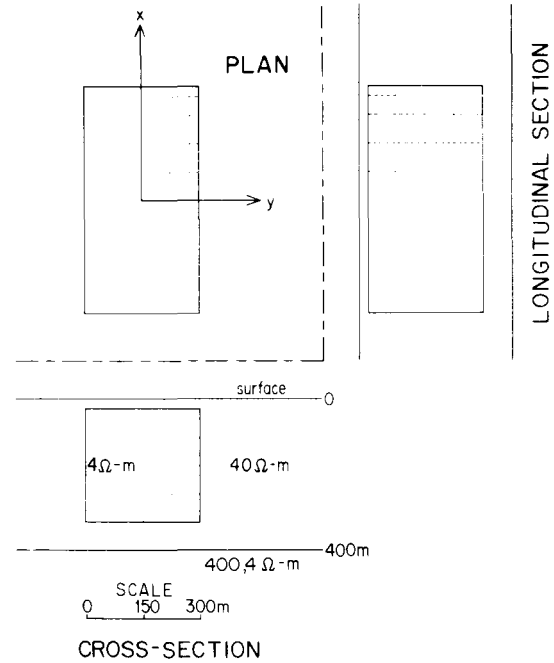
FIG. 2. Prismatic 3-D body in a two-layered earth used to represent small-scale, shallow structure. Dashes outline the discretization of the conductor into rectangular cells, shown only for the right half of the body in section and the upper right-hand quadrant in plan. Basal half-space resistivities of 400 and 4 $\Omega \cdot$ m are considered.

targets and can be extremely variable over distances of only a few hundred meters. This presents a grave sampling problem for MT measurements. Even if present 3-D modeling algorithms could accommodate this complex heterogeneity, which they cannot, it would be prohibitively expensive to record sufficient MT data to delineate its response. Thus, it becomes important to make increased use of MT response functions that are relatively insensitive to this sort of extraneous structure.

The second 3-D body we examine is intended to portray a sedimentary basin such as is frequently encountered in the Basin and Range province (Stewart, 1980; Eaton, 1982). These basins sometimes can be targets of investigations while at other times are of only secondary interest. Our particular model derives from study of the Milford Valley in southwestern Utah (Ward et al., 1978; Cook et al., 1981). However, gravity surveys suggest that the podiform geometry and overall dimensions of our model apply to the sedimentary fill of most grabens of the northern Basin and Range (Erwin and Berg, 1977; Erwin and Bittleston, 1977; Cook et al., 1981; Healy et al., 1981). Apart from relatively coarse-grained alluvium deposited from erosion of surrounding mountain ranges, many grabens contain large amounts of especially conductive, Pleistocene lacustrine clays (Stewart, 1980; Hintze, 1980). Also, we have studied the effects on MT response functions of a regional resistivity host to our basin model, a host which reflects tectonic setting and which may be close to one-dimensional to depths of tens of kilometers (Brace, 1971; Wannamaker, 1983).

We have disregarded inhomogeneities which are resistive compared to their layered hosts. Alteration by hydrothermal
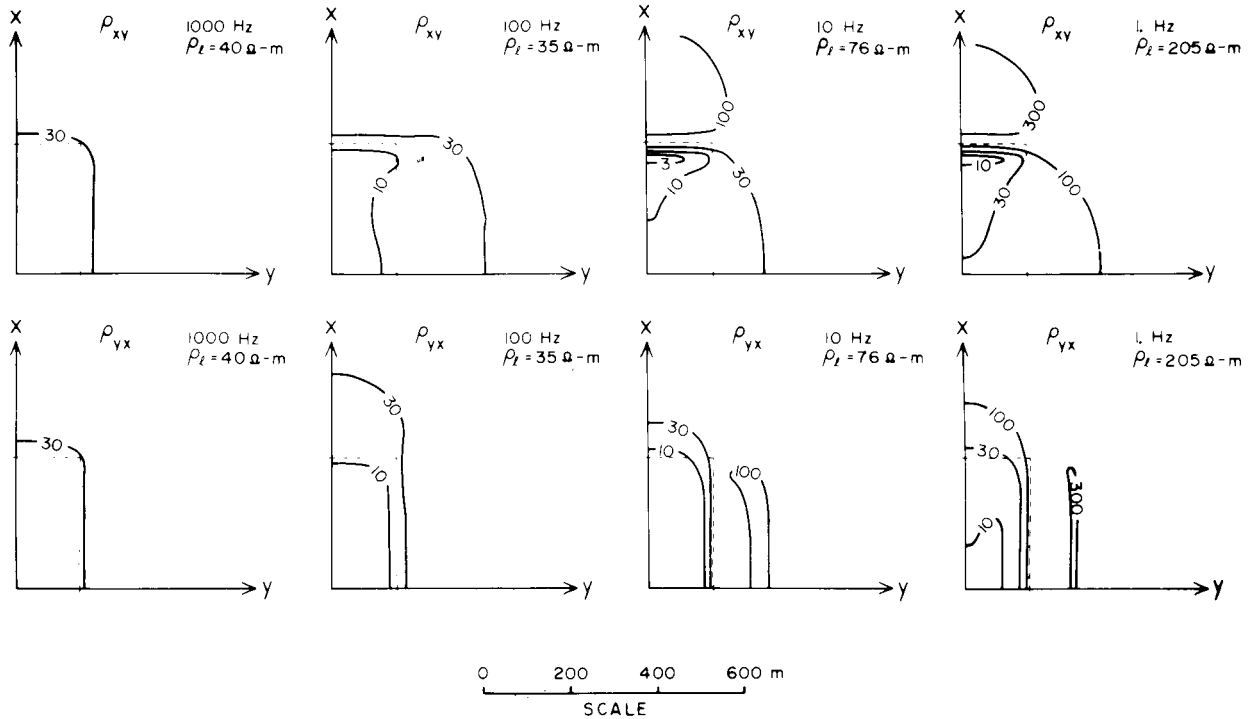
FIG. 3. Multifrequency plan maps of tensor apparent resistivities ρ_{xy} and ρ_{yx} over upper right-hand quadrant of the inhomogeneity of Figure 2. The body outline in plan is shown with dashes, the basal half-space resistivity is 400 $\Omega \cdot$ m and contour values are in $\Omega \cdot$ m. Also, the frequency and the value of the layered earth apparent resistivity ρ_ℓ are given in the upper right-hand corner of each plot.

brines discharging through rock is relatively conductive, although alteration by brines discharging through alluvium may be relatively resistive (e.g., Gamble et al., 1981). However, we consider distributions of sediments, due to their comparatively high porosity and clay contents, in general to be conductive structures in relatively resistive hosts (also Porath, 1971a; Hermance, 1982). Sedimentary basins form through erosion with collection of resulting detritus in topographic lows. In the northern Basin and Range, this concept is supported by the extensive gravity surveys cited previously. For areas where the existence of resistive bodies can be demonstrated, future model simulations certainly would be worthwhile.

The following MT responses were computed using the algorithm of Wannamaker et al. (1984), designed to model 3-D bodies in arbitrarily layered hosts with plane-wave incident fields. This algorithm is an extension of that developed by Ting and Hohmann (1981), which simulates the MT responses of 3-D structures in uniform half-spaces. Per Jones and Vozoff (1978), MT quantities are derived from total fields computed using two independent polarizations of $\mathbf{E}_i^0$. All calculations in the study were performed on the Prime 400 Series minicomputer of the Earth Science Laboratory of the University of Utah Research Institute.

The response of a small-scale structure

In Figure 2, a small, shallow conductive prism appears in a layer of overburden upon a resistive basement. The scattering current within the body was approximated by 48 rectangularly

prismatic cells to a quadrant. Contoured MT response functions shown next, with coordinate axes paralleling the axes of symmetry of the body, were derived from 92 variously spaced receiver points per quadrant and required about 4 hours CPU time for each frequency on the Prime 400. One hour CPU time on the Prime 400 compares to less than 20 s on a CRAY-1 without optimal vectorization.

Apparent resistivities and impedance phases.—The apparent resistivity signatures produced by our small-scale structure are displayed in Figure 3. Especially at the lower frequencies of 1. and 10 Hz where equation (14) becomes accurate and current-gathering is of particular importance, the anomalies are roughly electric dipolar in nature (Stratton, 1941, p. 431-434, p. 563-573), with undershoots and overshoots with respect to ρ_ℓ occurring over the ends of the body for ρ_{xy} and over the sides for ρ_{yx}. Note also at the lower frequencies that the anomalies are greater than those at 100 and 1 000 Hz. Boundary charges cause apparent resistivities to vary spatially by a factor of nearly 100, which is much higher than the body-host layer contrast, although such extremes are due partly to the abrupt nature of the resistivity contacts of the model and may be subdued for diffuse boundaries. It is most important, however, to realize that current gathering into conductive structure similar to our model will produce strong apparent resistivity anomalies that actually increase to a low-frequency asymptote as frequency falls. The results complement the study of Berdichevskiy and Dmitriev (1976), who considered a great variety of elliptically shaped, near-surface inhomogeneities but who con-
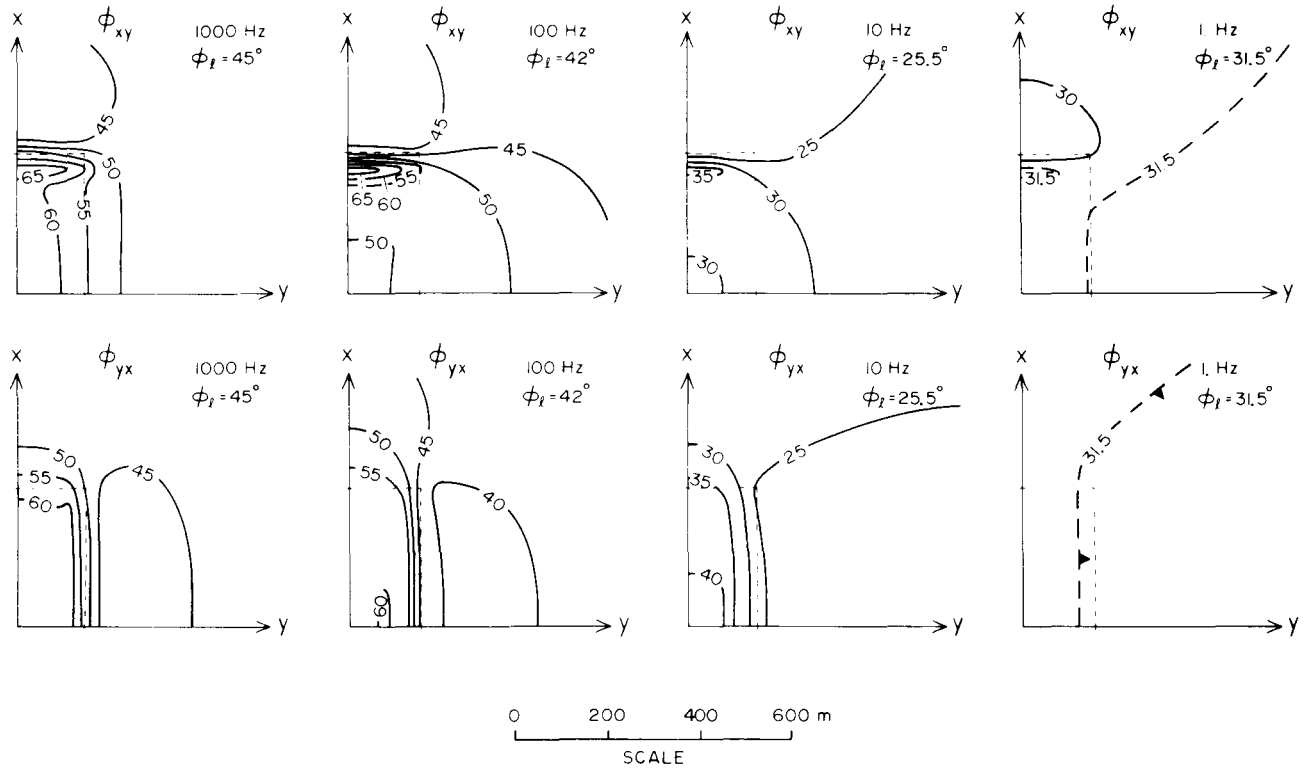
FIG. 4. Multifrequency plan maps of tensor impedance phases ϕ_{xy} and ϕ_{yx} over upper right-hand quadrant of the inhomogeneity of Figure 2. The body outline in plan is shown with dashes, the basal half-space resistivity is 400 $\Omega \cdot$ m and contour values are in degrees. Also, the frequency and the value of the layered earth impedance phase ϕ_ℓ are given in the upper right-hand corner of each plot.
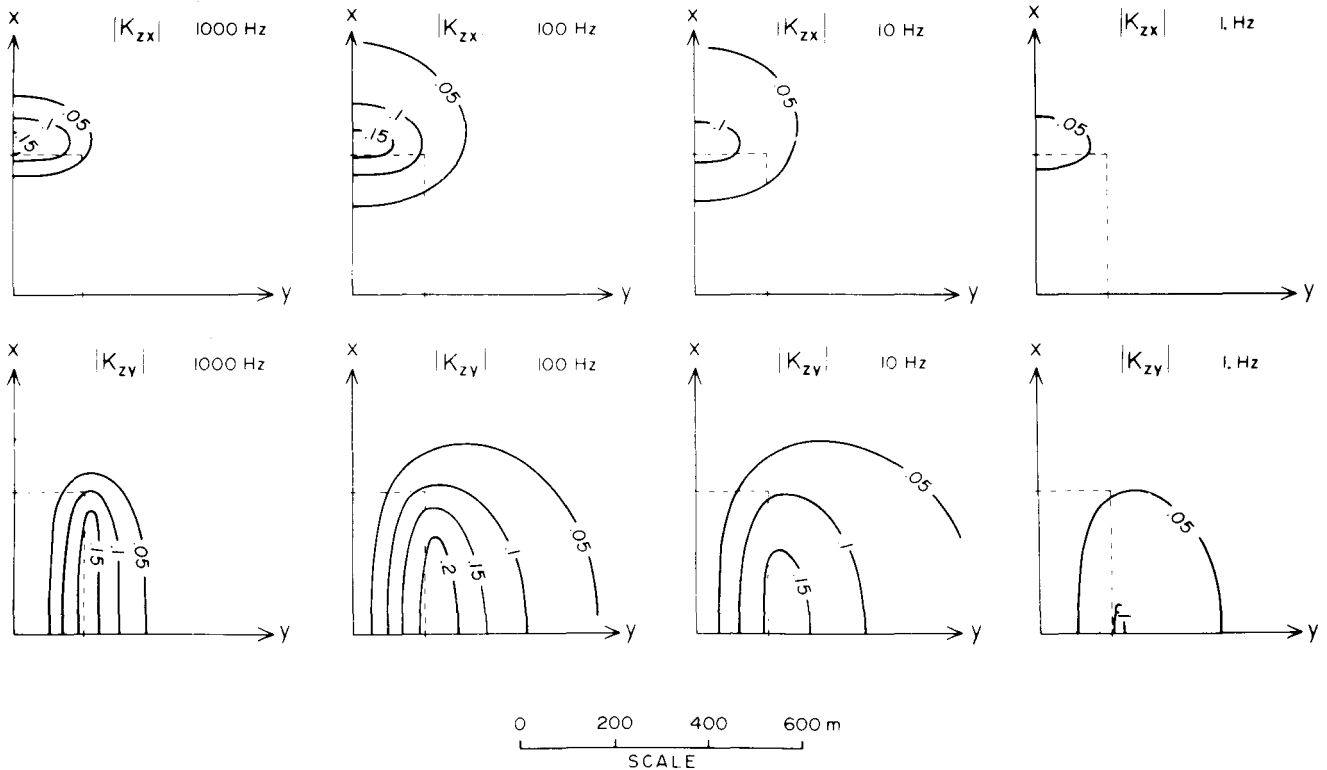
FIG. 5. Multifrequency plan maps of tipper element magnitudes $|K_{zx}|$ and $|K_{zy}|$ over upper right-hand quadrant of the inhomogeneity of Figure 2. The body outline in plan is shown with dashes, the basal half-space resistivity is 400 $\Omega \cdot$ m, and contour values are dimensionless.
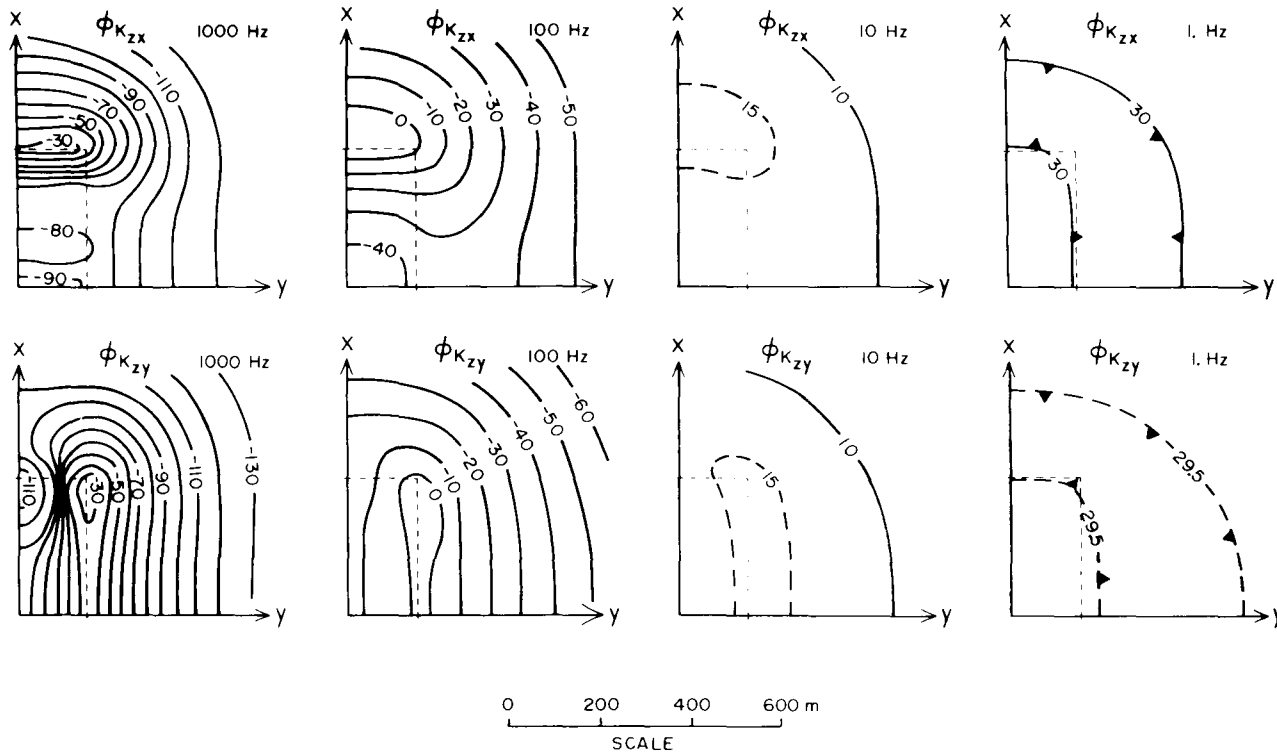
FIG. 6. Multifrequency plan maps of tipper element phases over upper right-hand quadrant of the inhomogeneity of Figure 2. The body outline in plan is shown with dashes, the basal half-space resistivity is 400 Ω · m, and contour values are in degrees.
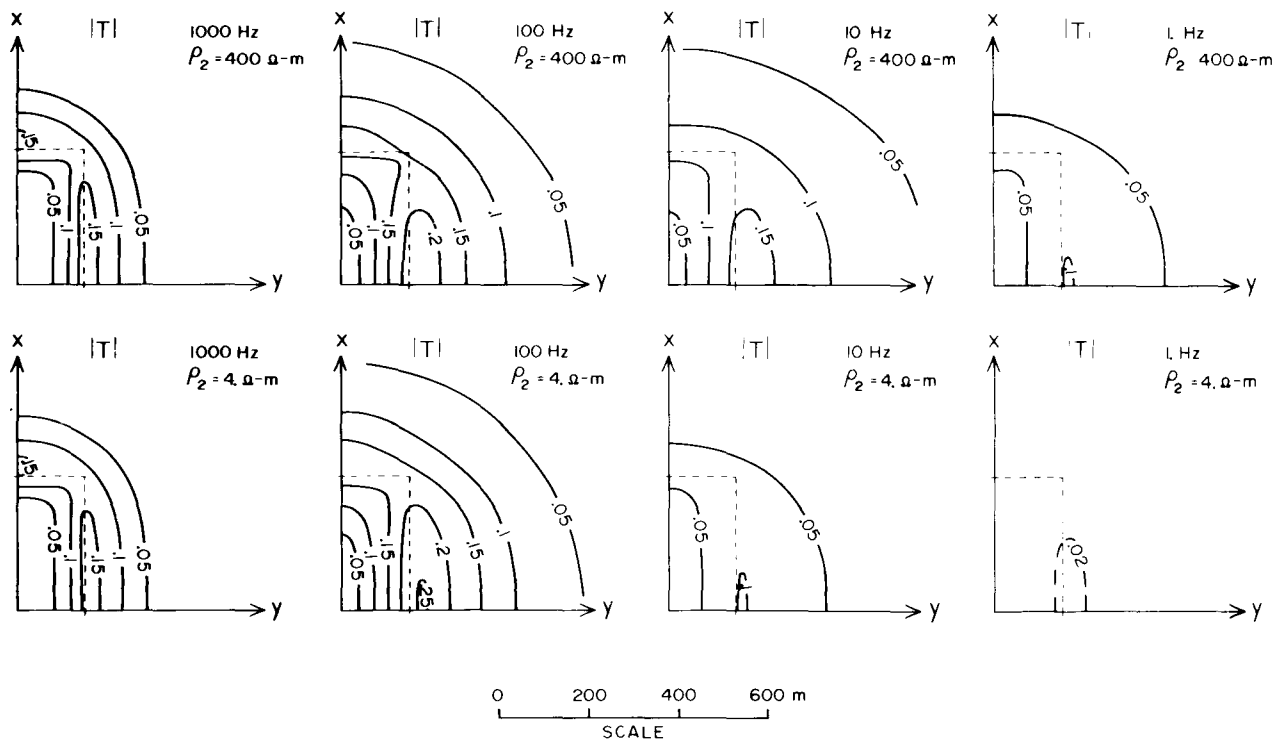
FIG. 7. Multifrequency plan maps of tipper magnitude | T | over upper right-hand quadrant of the inhomogeneity of Figure 2. The body outline is shown in plan with dashes and the contours are dimensionless. Basal half-space resistivities of 400 and 4 Ω · m, identified in the upper right-hand corner of each plot, have been considered in the upper and lower rows of diagrams.

fined their attention to only the low-frequency limits of the distortions due to such inhomogeneities.

Behavior of the impedance phase is entirely different from that of the apparent resistivities, as seen in Figure 4. At 100 and 1 000 Hz, departures may appear in excess of 20 degrees from the layered host phase ϕ_ℓ, which is labeled in the upper right corner of each panel of the figure. At 1. Hz, on the other hand, the secondary electric field is essentially in phase with the incident E-field and the total and incident H-fields are very nearly equal, so that impedance phase values deviate less than 3 degrees from ϕ_ℓ. Impedance phase anomalies due to our model of small-scale, extraneous structure peak at high frequencies, certainly in excess of 100 Hz, and contribute negligibly to observed phase responses below 1. Hz.

Tipper transfer function.—Peak amplitudes of around 0.15 for $|K_{zx}|$ and 0.20 for $|K_{zy}|$ at 100 and 1 000 Hz over this conductor are illustrated in Figure 5. At 1. Hz, because of the appearance of Z_ℓ in equation (18), values of $|K_{zy}|$ have decreased markedly and barely reach 0.10. Complicated anomalies in the phase of elements of $[\tilde{K}_z(\mathbf{r})]$ are seen in Figure 6 at 100 and 1 000 Hz. At distance from the body at these higher frequencies, the rather uniform spacing of the phase contours represents an outwardly propagating secondary wavefront from this essentially electric dipole scatterer. Beyond several hundred meters, however, the contour spacing broadens, indicating we are approaching the far-field where secondary wavefronts become transverse electromagnetic (TEM) to z. Phases at 1. Hz, as foretold by equation (18), have approached the layered earth impedance phase $\phi_\ell = 31.5$ degrees. In conclusion, responses in both magnitude and phase of elements of $[\tilde{K}_z(\mathbf{r})]$ due to this sort of small-scale structure are most important at frequencies above 100 Hz.

Figure 7 illustrates the effect of the layered host on $[\tilde{K}_z(\mathbf{r})]$. At 100 and 1 000 Hz, anomalies in tipper for a conductive basement of 4 $\Omega \cdot$m are essentially identical to those for a resistive basement of 400 $\Omega \cdot$ m, since at these high frequencies, $[\tilde{Q}_s^0(\mathbf{r})]$ and $[\tilde{Z}_\ell]$ are insensitive to ρ_2. Significant differences are apparent at 1. Hz, however, with peak anomalies for $\rho_2 = 400 \ \Omega \cdot$m being greater by a factor of about $4\frac{1}{2}$ than those for $\rho_2 = 4 \ \Omega \cdot$ m. This factor is close to the ratio of the magnitudes of the layered earth impedance at 1. Hz for the two layered hosts, as explained by equation (18). One-dimensional hosts with layer resistivities that increase with depth, through their effect on $[\tilde{Z}_\ell]$ as discussed with equation (9), tend to prolong the anomalies in $[\tilde{K}_z(\mathbf{r})]$ to lower frequencies than do layered hosts that become more conductive with depth.

The response of sedimentary basins

An accumulation of Basin and Range graben alluvial fill is depicted in Figure 8 as a large, plate-like inhomogeneity. Although outcropping in nature, this model valley is buried 500 m to obtain accurate results with the integral equations algorithm (Ting and Hohmann, 1981). A model one-dimensional host for this basin, similar to those of Brace (1971) or Wannamaker (1983), also is illustrated in Figure 8. The scattering current in this model was approximated by 110 rectangularly prismatic cells per quadrant and as many as 195 receiver points per quadrant were used to construct upcoming plots. Results required about 20 hours CPU time for each frequency on the Prime 400.
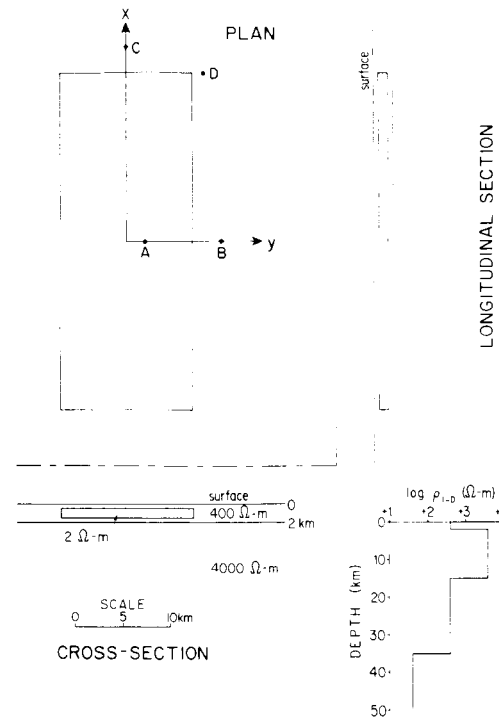
FIG. 8. Plate-like 3-D body in a four-layered earth representing a sedimentary basin in the Basin and Range tectonic province of the western United States. Dashes outline the discretization of the conductor into rectangular cells, shown only for the right half of the body in section and the upper right-hand quadrant in plan. The 1-D resistivity host for this basin model is shown toward the lower right and four points at which sounding curves were computed are given in the plan view.

Regional current gathering.—To begin, we study the widespread distortion of electric fields in the vicinity of our model of a sedimentary basin. Figures 9 and 10 contain plan views of total electric field polarization ellipses at 0.032 Hz over one quadrant of the basin for x- and y-directed polarizations of $\mathbf{E}_i^0$. This is a fairly low frequency for this scale of structure and the response is largely near-field or galvanic, so the ellipses are almost linear.

A clear display of regional current gathering appears in Figure 9, showing the undershoot-to-overshoot, electric dipolar behavior of the ellipses expected over the end of a 3-D body for this orientation of $\mathbf{E}_i^0$. With the incident field directed along the x-azis, a regional depression of $\mathbf{E}_h^0(\mathbf{r})$ occurs to the side of the basin in the y-direction. Outside the corner of the prism, very large values of $\mathbf{E}_h^0(\mathbf{r})$ occur, locally exceeding twice the incident E-field and indicating current convergence from a large volume of the host toward the smaller end of the basin.

The electric field ellipses in Figure 10 for a y-oriented incident E-field show behavior complementary to those in Figure 9. The electric dipolar character of the ellipses is evident over the side of the body for this polarization of $\mathbf{E}_i^0$, in particular causing a regional amplification of $\mathbf{E}_h^0(\bar{\mathbf{r}})$ to the side of the basin in the y-direction. Very small E-fields appear directly over the model for both polarizations of $\mathbf{E}_i^0$, with the y-directed incident field giving a somewhat more extreme anomaly.

Specific effects of the layering upon regional current gathering can be demonstrated in longitudinal section views. In

X

► y

0   4   8 km $\vec{E}_{i1}$ ─

SCALE
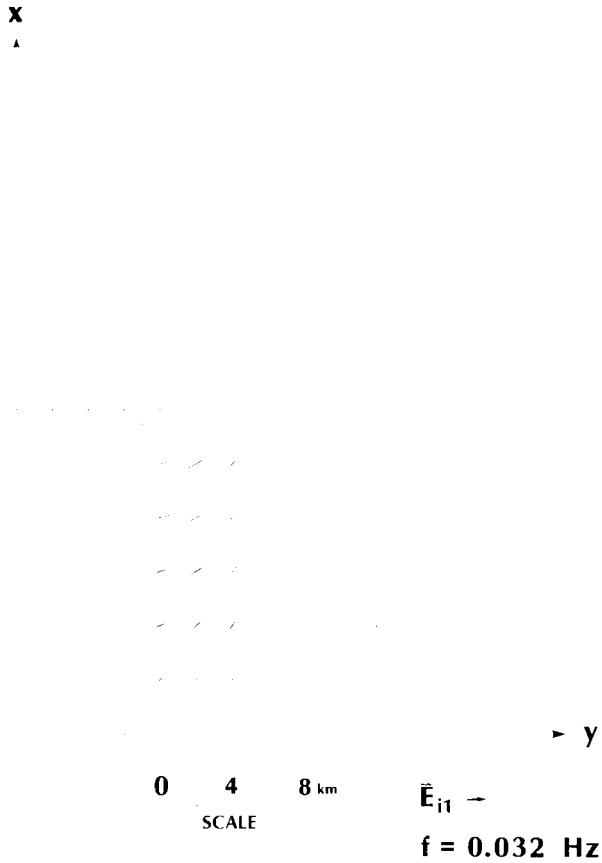
f = 0.032 Hz

FIG. 9. Plan view of total E-field polarization ellipses over upper right-hand quadrant of basin model at 0.032 Hz for an x-directed incident field. The magnitude of the linearly polarized $\mathbf{E}_i^0$ is shown in the lower right-hand corner of the diagram.

X

► y

0   4   8 km $\vec{E}_{i2}$ ─

SCALE
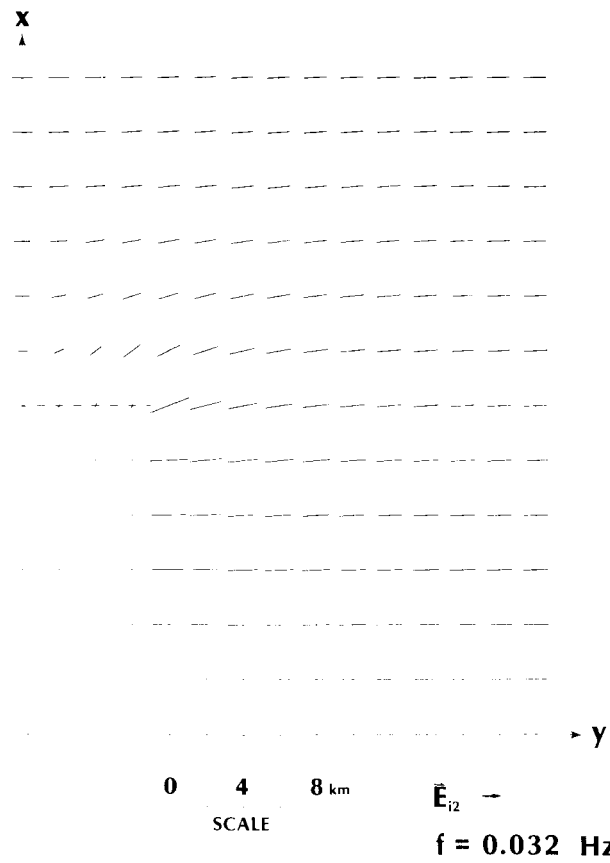
f = 0.032 Hz

FIG. 10. Plan view of total E-field polarization ellipses over upper right-hand quadrant of basin model at 0.032 Hz for a y-directed incident field. The magnitude of the linearly polarized $\mathbf{E}_i^0$ is shown in the lower right-hand corner of the diagram.

Figure 11, the basin model resides in a uniform half-space of 400 $\Omega \cdot$ m and total electric field polarization ellipses have been computed, again at 0.032 Hz, to a depth in excess of 20 km. The approximately electric dipolar character of $\mathbf{E}^0(\mathbf{r})$ in longitudinal section is apparent, where boundary charges result in current from great depth gathering up to the valley. As in the plan views involving the layered host, very large values of total E-field are seen near the ends of the plate. The undershoot-to-overshoot behavior of $E_{xs}^0(\mathbf{r})$ drawn at the top of the figure is another view of this phenomenon. At lateral distances near 40 km from the prism's center, $|E_{xs}^0(\mathbf{r})|$ has decayed to about 5 percent of E_{xi}^0.

In Figure 12, the model is returned to its four-layered host and E-field polarization ellipses are again calculated. In the uppermost 400 $\Omega \cdot$ m layer containing the basin model the ellipses are nearly horizontal and attenuate with distance much more slowly than in the case of the half-space host. The plot of $E_{xs}^0(\mathbf{r})$ in the upper part of the figure supports this, with $|E_{xs}^0(\mathbf{r})|$ at lateral distances near 40 km from the plate's center exceeding 20 percent of $|E_{xi}^0|$. To comprehend this relatively slow attenuation, one must realize that secondary currents induced in the 400 $\Omega \cdot$ m layer about the basin have difficulty penetrating the more resistive 4 000 $\Omega \cdot$ m medium, and hence can decay geo-

metrically most easily in just the x-y plane (Wannamaker et al., 1984). By contrast, secondary currents about the basin in the uniform 400 $\Omega \cdot$ m half-space can die away readily in the z-direction as well. Hence, the surface anomaly in Figure 12 is observed to be important to greater distances from the body than is that in Figure 11.

However, despite the fact that secondary current flow about the basin in the four-layered earth has difficulty penetrating the 4 000 $\Omega \cdot$ m medium, electric field ellipses in this most resistive layer in Figure 12 exhibit much stronger vertical components than those at comparable depths in the 400 $\Omega \cdot$ m half-space in Figure 11. This phenomenon is due to the preservation of the normal component of current density across layer interfaces, which in turn means that the vertical component of secondary electric field experiences a step jump by a factor of ten going from the 400 $\Omega \cdot$ m layer down to the 4 000 $\Omega \cdot$ m layer (note there is no vertical component of the primary field). Nevertheless, we emphasize that values of secondary current density in the 4 000 $\Omega \cdot$ m material are actually much smaller than values at corresponding positions in the less resistive, 400 $\Omega \cdot$ m half-space host. Confirming this is the very flat nature of the ellipses in Figure 12 in the deep 400 $\Omega \cdot$ m layer extending from 15 to 35 km, showing that deep regional current flow is essentially insu-
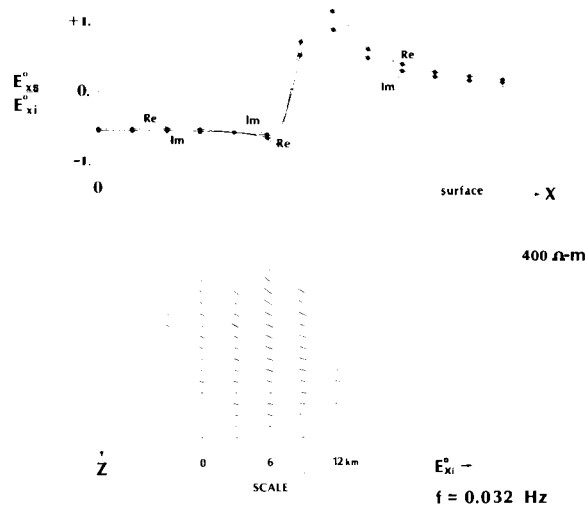
FIG. 11. The basin model is enclosed in a $400\ \Omega \cdot m$ half-space for this section view of total E-field polarization ellipses through one half of the basin at 0.032 Hz. The incident field is linearly polarized in the x-direction and its magnitude at the surface is shown in the lower right-hand corner of the diagram. At the top of the figure are profiled real and imaginary components of $\mathbf{E}^0_{xs}(\mathbf{r})$ normalized by $|\mathbf{E}^0_{xi}|$.
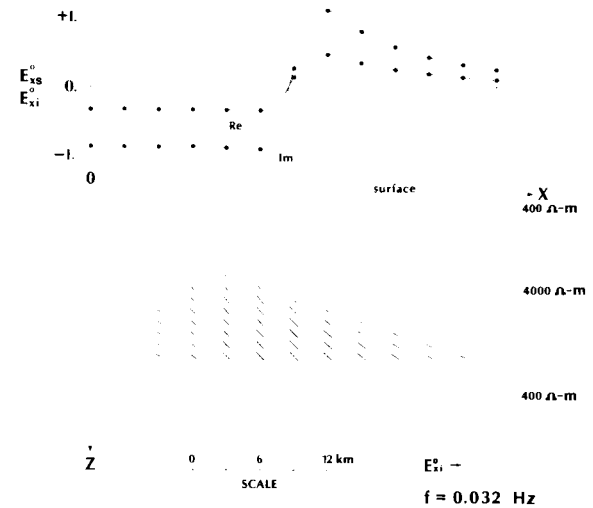
FIG. 12. The basin model is returned to the four-layered host for this section view of total E-field polarization ellipses at 0.032 Hz. The incident field is again linearly polarized in the x-direction and its magnitude at the surface is shown in the lower right-hand corner of the diagram. At the top of the figure are profiled real and imaginary components of $\mathbf{E}^0_{xs}(\mathbf{r})$ normalized by $|\mathbf{E}^0_{xi}|$.

lated by the 4 000 $\Omega \cdot m$ layer from the effects of the conductive basin.

Effects of the layered host upon electric field anomalies carry over to the apparent resistivity signatures (Ranganayaki and Madden, 1980). In Figure 13, ρ_{xy} and ρ_{yx} have been plotted for a frequency of 0.032 Hz along the y-axis of the 3-D basin model, with both half-space and layered hosts being considered. To the side of the basin within either host, an apparent resistivity anisotropy in excess of an order of magnitude is observed; it diminishes with distance from the body. With the half-space host, neither ρ_{xy} nor ρ_{yx} depart more than 10 percent from the 1-D sounding ρ_ℓ beyond distances of about 25 km from the center of the basin. However, the apparent resistivity anomalies about the basin in the layered host exist to considerably greater distances than this. With the layered sequence, ρ_{xy} and ρ_{yx} do not lie within 10 percent of the ρ_ℓ at this frequency until about 60 km from the center of the basin, which is well off our diagram. We conclude that in the interpretation of MT soundings in the Basin and Range province, not only must one be aware of the sedimentary basin immediately adjacent to the soundings, but perhaps also of basins at greater distances.

Magnetotelluric strike estimations.—Principal coordinate directions of tensor MT response functions provide measures of preferred geoelectric trends. In Figure 14 are plotted off-diagonal impedance polar diagrams as well as tipper-strike directions for a variety of receivers over and around the basin model at 0.032 Hz. Our definition of tipper-strike is the x-axis for which $|K_{zy}|$ is maximized. The length of the tipper-strike bars is proportional to tipper magnitude. Since $|T|$ is zero directly over the model, no tipper-strike can be defined here.

From the impedance polar diagrams, one sees that principal axes of $[\mathbf{Z}(\mathbf{r})]$ occur approximately every 90 degrees, so that
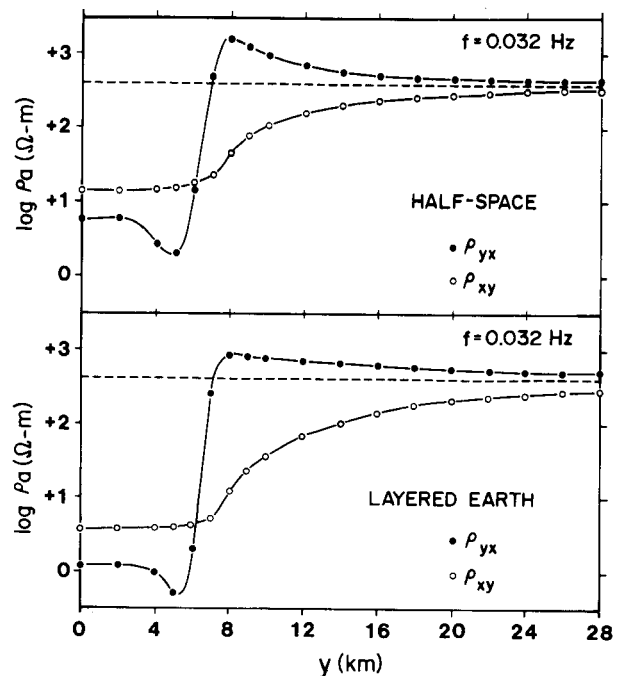
FIG. 13. Profiles of ρ_{xy} and ρ_{yx} along the y-axis over the 3-D basin model computed for a frequency of 0.032 Hz. The response over the basin in a uniform $400\ \Omega \cdot m$ half-space appears in the top half of the diagram for comparison to the response over the basin in the layered host of Figure 8. The 1-D host apparent resistivity ρ_ℓ also has been plotted with dashes for reference for both the half-space and the layered earth.

Z_{xy}

K_z-strike

$(|T| = 0.1)$

0 2 4 6 8
SCALE
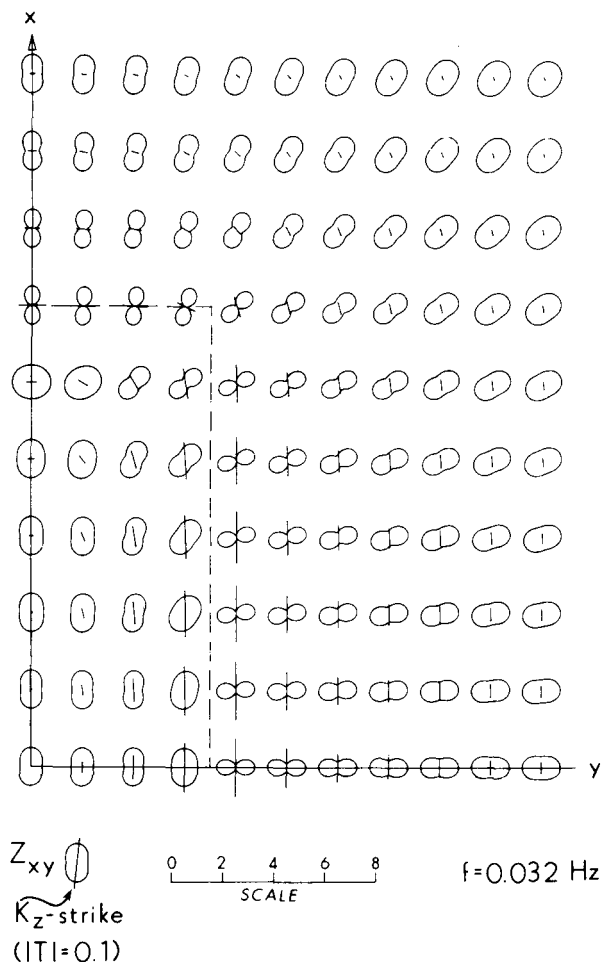
f = 0.032 Hz

FIG. 14. Plan view of tipper-strike and off-diagonal impedance polar diagrams over the upper right-hand quadrant of the basin model for a variety of receivers at 0.032 Hz. Length of the tipper-strike bars is proportional to magnitude of tipper, exemplified by a value of $|T| = 0.1$ in the key.
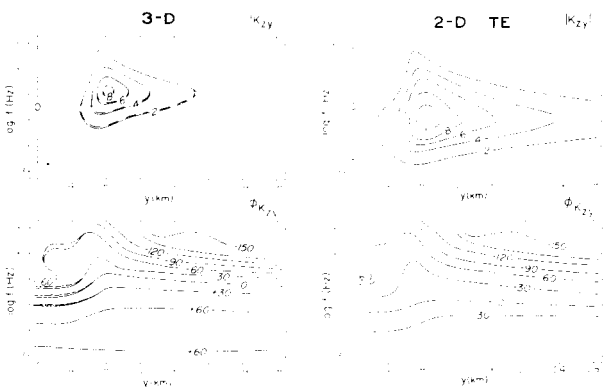
FIG. 15. Pseudosections of magnitude and phase of K_{zy} for profiles at $x = 0$ (solid contours) and $x = 9$ (dashed contours) over the 3-D basin model compared to 2-D TE pseudosections for corresponding model of infinite strike length. Pseudosections commence at $y = 0$ over the center of the basin and extend in the y-direction. Contours of magnitude and phase are, respectively, dimensionless and in degrees.

they alone cannot give unique strike directions (Word et al., 1970; Vozoff, 1972). Tipper-strike parallels more closely the true limits, both sides and ends, of the valley than does the principal axis of $[\tilde{Z}(r)]$ closest to tipper-strike (cf., Jones and Vozoff, 1978). Principal axes of the impedance also seem to be a less stable indicator of geoelectric trends just inside the basin.

Over single inhomogeneities such as that of Figure 8, we conclude that tipper-strike is somewhat superior to the principal axes of the impedance due to its closer conformity to true geoelectric trends, its greater stability and its lack of a 90 degree ambiguity. Nevertheless, both types of trend estimator show reasonably close agreement overall, especially to the side of the valley, and thus are considered largely equivalent for single simple bodies.

Tipper pseudosections.—Multifrequency calculations of tipper element K_{zy} were performed along two traverses over the 3-D basin and are compared in Figure 15 to calculations over a 2-D model of identical cross-section (Rijo, 1977; Stodt, 1978). For display in pseudosection form, log frequency and the y-axis serve as ordinate and abscissa for contour plots of amplitude and phase (Vozoff, 1972). The 3-D traverses reside along the line $x = 0$, over the prism's center, and along $x = 9$ km, halfway to the prism's end. For the pseudosection displays, the x-y coordinates of the MT response functions parallel the plate symmetry axes. In this manner, K_{zy} over the 3-D model can be compared to the 2-D transverse electric responses.

Pseudosection contours were constructed from computations at every half decade in frequency, from 0.001 to 100 Hz. However, we distrust the numerical accuracy of the 3-D calculations above 10 Hz for this large body, although the discretization we have chosen is as fine as is practical with our computer. Since 3-D and 2-D values of all MT functions presented have converged by the point that frequency has risen to 10 Hz, 3-D contours at higher frequencies were derived by extrapolation using 2-D results.

In Figure 15, agreement in $|K_{zy}|$ between the profiles at $x = 0$ and at $x = 9$ km over the 3-D body is close at all frequencies. However, a significant departure from the 2-D transverse electric responses occurs below 3 Hz, with the 3-D values at lower frequencies being greatly subdued by comparison. To understand this 3-D anomaly, consider the regional depression of $E_t^0(r)$ occurring over and beside the valley when E_i^0 is x-oriented (Figure 9). The depression results overwhelmingly from boundary charges on the ends of the 3-D prism and reaches a maximum at low frequencies. These charges effect a reduction of J_x within, and hence $[\tilde{Q}_{rs}^0(r)]$ over, the 3-D basin. In contrast, the lack of charges on the 2-D body allows a strong 2-D TE response in $|K_{zy}|$ over a broader frequency range.

The magnitude of K_{zy} over the 3-D basin model peaks at a frequency near 1. Hz. Both 2-D and 3-D amplitudes of $|K_{zy}|$ decay rapidly at frequencies below 0.03 Hz in Figure 14, a result of the resistivity of the layered host decreasing at depths beyond 15 km, so that $|Z_t|$ in equation (18) attenuates quickly at these lower frequencies. Due to this phenomenon, and in light of the strength of the 2-D response, we conclude that large amplitudes of tipper will occur over long, high contrast bodies in hosts that have layer resistivities increasing with depth.

Agreement between 2-D and 3-D phases of K_{zy} in Figure 15 is limited to quite high frequencies, above 10 Hz for this model. The inclination of phase contours away from the valley above about 1. Hz is another view of outwardly traveling secondary

waves, and corresponds to the rather uniform spacing of contours on single frequency plan maps such as Figure 6. At low frequencies for both 2-D and 3-D valley models, phases of K_{zy} approach the phase of the layered host impedance ϕ_r, which is near 60 degrees at 0.003 Hz.

The separation in frequency of the responses of $[\tilde{\mathbf{K}}_z(\mathbf{r})]$ for the basin model and for the small-scale structure, apparent by comparison of Figures 5, 6, and 15, is fundamentally a demonstration of EM scaling in MT responses (Stratton, 1941, p. 488–490; Grant and West, 1965, p. 478–482). In the concept of EM scaling, small inhomogeneities can have MT responses as strong as those of large ones. However, provided corresponding resistivities and aspect ratios are similar, the small and large body responses have frequency dependencies that are separated as the square of the geometric scale factor distinguishing the different bodies. Specifically, then, examination of observed tipper may be a quick and easy means of identifying the presence of any large, buried resistivity anomaly, constituting perhaps an exploration target, beneath small-scale extraneous structure. For estimating geoelectric trends of basin sediments like the model we have considered, tipper-strike should be computed in the frequency range 0.1 to 1. Hz to ensure that the basin response in $[\tilde{\mathbf{K}}_z(\mathbf{r})]$ is strong while that of any small-scale, extraneous structure is attenuated.

Nevertheless, it is possible that resistivity structure of a scale significantly greater than that of typical Basin and Range graben sediments, for instance resulting from regional thermotectonic perturbations common to this province (Eaton, 1982), can dominate tipper amplitudes at frequencies of 0.01 Hz or below (consider Porath, 1971b). This underscores the need for care in defining the term "regional structure" and thus to impose a selective weighting with respect to frequency of one's tipper-strike estimates (compare Gamble et al., 1982). Given the dependence of tipper responses on both the properties of the body and of the layered host, use of an algorithm like that of Wannamaker et al. (1984) is recommended for assessment of this weighting.

Apparent resistivity and impedance phase pseudosections.—As was done for the tipper, apparent resistivities ρ_{xy} and ρ_{yx} as well as impedance phases ϕ_{xy} and ϕ_{yx} have been displayed in pseudosection form in Figures 16 and 17. A strong discrepancy between 2-D TE and corresponding 3-D responses, designated ρ_{xy} (3-D) and ϕ_{xy} (3-D), for our basin model is illustrated again in Figure 16, this time for frequencies below about 1. Hz. This apparent resistivity over and adjacent to the 3-D plate decreases as frequency falls relative to the apparent resistivity of the layered host ρ_r, which the 3-D response approaches at large distances from the valley. Correspondingly, anomalously high values of ϕ_{xy} (3-D) appear in the vicinity of the body, although the discrepancy between this quantity and the host impedance phase ϕ_r is less than 5 degrees outside the valley below 0.03 Hz and less than 5 degrees anywhere below 0.003 Hz. In contrast, ρ_{xy} (2-D) falls with respect to ρ_r, while ϕ_{xy} (2-D) surpasses ϕ_r only above 0.3 Hz with just the opposite behavior at lower frequencies.

This 3-D anomaly may be explained again in terms of boundary charges, acting on ρ_{xy} and ϕ_{xy} through equations (12) and (14b). Such charges do not occur in the 2-D body for this transverse electric mode, so that the wave equation for $\mathbf{E}_s(\mathbf{r})$ approaches the homogeneous Laplace's equation at lower frequencies and there is a diminishing contribution by the secondary E-field to the anomalous ρ_{xy} and ϕ_{xy}. In fact, the 2-D TE responses below about 0.1 Hz result predominantly from a strong secondary H-field, which remains important as governed by equations (8) and (12) until frequencies under 0.001 Hz for the 2-D basin model. On the other hand, over the 3-D model at frequencies less than 0.1 Hz, $\mathbf{H}_{hs}^0(\mathbf{r})$ is much smaller than that over the 2-D counterpart. Once more, boundary charges severely depress the scattering current within, and thus $[\tilde{\mathbf{Q}}_{hs}^0(\mathbf{r})]$ over, the 3-D body relative to the 2-D structure. Hence, ρ_{xy} and ϕ_{xy} for the 3-D basin model arrive at low-frequency asymptotes around 0.003 Hz.

If our model is representative of graben sedimentary fill in the Basin and Range, then 2-D transverse electric modeling
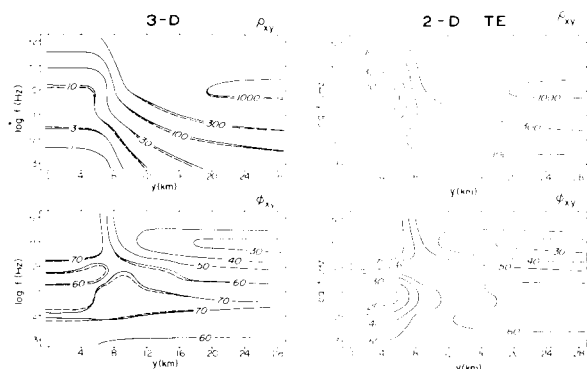
FIG. 16. Pseudosections of ρ_{xy} and ϕ_{xy} for profiles at $x = 0$ (solid contours) and $x = 9$ km (dashed contours) over the 3-D basin model compared to 2-D TE pseudosections for corresponding model of infinite strike length. Pseudosections commence at $y = 0$ over the center of the basin and extend in the y-direction. Contours of ρ_{xy} and ϕ_{xy} are in $\Omega \cdot$ m and degrees.
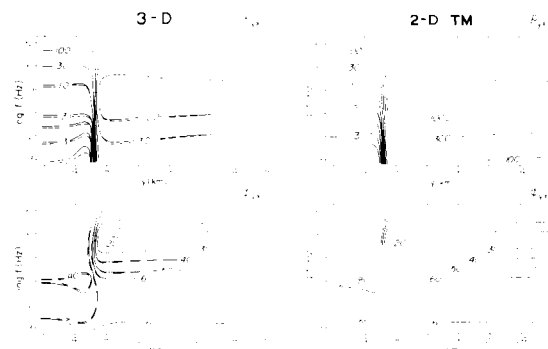
FIG. 17. Pseudosections of ρ_{yx} and ϕ_{yx} for profiles at $x = 0$ (solid contours) and $x = 9$ km (dashed contours) over the 3-D basin model compared to 2-D TM pseudosections for corresponding model of infinite strike length. Pseudosections commence at $y = 0$ over the center of the basin and extend in the y-direction. Contours of ρ_{yx} and ϕ_{yx} are in $\Omega \cdot$ m and degrees.

algorithms may result in erroneous resistivity cross-sections when applied to apparent resistivities and impedance phases identified as TE in this province. In attempting to replicate the 3-D response in Figure 16 with a 2-D TE routine, one would need to place false low resistivities at some depth below the true basin. Further errors through use of 2-D TE programs will likely occur if small-scale, near-surface structure such as we have simulated in Figure 2 is widespread (for example, see Wannamaker et al., 1978).

Given the size of the basin model, the frequencies at which 2-D TE and corresponding 3-D MT responses agree closely may seem surprisingly high. Wannamaker et al. (1984), however, explained that the length a 3-D body must have to achieve agreement with 2-D TE components depends strongly on the 1-D host, with bodies in layers overlying resistive basements needing to be longer than bodies overlying conductive basements. Layered host resistivities in nature increase with depth in the upper several kilometers (Brace, 1971; Wannamaker, 1983), exacerbating the difficulties with 2-D TE interpretations.

In contrast to the responses depicted in Figure 16, anomalies in ρ_{yx} and ϕ_{yx} in Figure 17 are essentially the same for the two 3-D traverses and the 2-D profiling at all frequencies. Some minor differences right over the valley at lower frequencies will be explained with the presentation of sounding curves. The reasons for this agreement are twofold. First, no secondary H-field exists for the 2-D TM mode (Swift, 1967), and there is only an insignificant contribution by $H_s^0(\mathbf{r})$ to the corresponding 3-D response. Second, boundary charges on the sides of the basin are included in both 2-D TM and 3-D formulations. These boundary charges in turn lead to current gathering into the sides of the 2-D and 3-D basin models. As was demonstrated for the 3-D model in Figure 10, such current gathering is manifested in the development of a crudely dipolar variation in the electric field over the basin toward lower frequencies. Low-frequency asymptotes to ρ_{yx} and ϕ_{yx} are reached by about 0.01 Hz outside the basin model. In contrast, these asymptotes directly over the model do not occur until about 0.001 Hz due to the tendency of the secondary and incident electric fields to cancel here.

As was the case for the tipper, the frequency dependence of both ρ_{xy} and ρ_{yx} as well as anomalous values of both ϕ_{xy} and ϕ_{yx} for the basin model occur over a much lower frequency range than for the small-scale, near-surface model of Figure 2. This result is a further manifestation of EM scaling in MT responses. Thus, examination of observed impedance phases may be another straightforward means of identifying the presence of any large, buried resistivity anomaly, constituting perhaps an exploration target, beneath small-scale extraneous structure.

We infer from Figure 17 that accurate cross-sections of earth resistivity may be interpreted from profiles of MT measurements across elongate, geometrically regular 3-D bodies using a 2-D transverse magnetic algorithm. For 2-D TM modeling of field data, we recommend tipper-strike for specifying a fixed coordinate system for the MT response functions. Tipper-strike is a stable, unambiguous strike estimator that conforms closely to true geoelectric trends. Use of $[\tilde{\mathbf{K}}_z(\mathbf{r})]$ to define the coordinate axes will result in pseudosections that are essentially identical to those in Figures 16 and 17, with the possible exception of field points close to the center of the model. These latter axes may be constrained to be consistent with the majority of the

strike estimates. For single simple bodies such as our valley model, however, principal axes of $[\tilde{\mathbf{Z}}(\mathbf{r})]$ probably are satisfactory also for this purpose.

On the other hand, telluric distortions in any near-surface extraneous structure such as modeled in Figure 2 may cause scatter from sounding to sounding in the principal axes of $[\tilde{\mathbf{Z}}(\mathbf{r})]$ from their orientations over the basin alone. The resulting nonuniform coordinate system leads to variations specifically in the impedance phase ϕ_{yx}, and in the frequency dependence of the apparent resistivity ρ_{yx}, of high spatial frequency occurring at middle to low angular frequencies. These variations in turn are due to the sedimentary basin, which has induced a broad anisotropy in both ϕ_{xy} and ϕ_{yx}, and in the frequency dependence of both ρ_{xy} and ρ_{yx}, at middle to low frequencies. A nonuniform coordinate system mixes secondary field components of differing phases in differing proportions from sounding to sounding, thus leading to inconsistent complex quantities. These rapid spatial variations in ϕ_{yx} and in the frequency dependence of ρ_{yx}, since they occur at middle and low frequencies, would be difficult if not impossible to fit with a 2-D TM algorithm. As discussed previously, tipper-strike remains relatively uniform in the face of small-scale extraneous structure and therefore is superior to the principal axes of the impedance for coordinate system definition.

It should be emphasized that use of a 2-D transverse magnetic algorithm as we propose it is no interpretive panacea. For example, consider a buried 3-D dike-like conductive inhomogeneity elongated in the x-direction. If the dike is thin compared to its depth, the measured response in ρ_{yx} and ϕ_{yx} may be very weak (Vozoff, 1972), even though it can be modeled with a 2-D TM routine. On the other hand, if the strike extent of the dike is large compared to its depth, a strong response in ρ_{xy} and ϕ_{xy} may exist. However, this response requires a full 3-D interpretation including the effects of current gathering. Also, apart from employing MT strike estimations in transverse magnetic mode identification, this 2-D TM approach can make no use of the tipper.

Furthermore, if a 3-D structure is highly irregular in geometry, then application of a 2-D TM algorithm can be hazardous (Hermance, 1982). In such instances, however, we doubt the validity of 2-D TE approaches as well. To us, the gravity surveying of the northern Basin and Range cited previously suggests that most graben sedimentary fill is podiform, with limited electrical connection between basins. MT interpretation certainly should be approached on a case-by-case basis to avoid errors due to unwarranted generalizations. Nevertheless, 2-D TM modeling can be exploited to the fullest given careful MT survey design at the outset utilizing independent constraints such as gravity and geology.

Apparent resistivity and impedance phase soundings.—To explore the applicability of 1-D interpretation schemes for 3-D data, in Figures 18 through 21 we present principal apparent resistivity and impedance phase soundings for positions A, B, C, and D of Figure 8. In a manner similar to that for the pseudosections, the transverse electric mode has been associated with ρ_{xy} and ϕ_{xy} by selecting the principal direction of the impedance which is closest to tipper-strike as the x-axis of the principal coordinate system (Word et al., 1970; Vozoff, 1972). Definition of modes in this manner is common practice although strictly speaking, the EM fields scattered by 3-D bodies

do not decouple into TE and TM modes (Swift, 1967). Note in Figure 14 that this principal axis swings, from a direction paralleling the x-axis of symmetry of the basin model for points A and B, counterclockwise about 40 degrees for site D until finally it parallels the y-axis of symmetry of the basin for site C.

At point A over the basin model, principal apparent resistivities and impedance phases for the 3-D body are compared in Figure 18 to a 1-D response which would occur if the 2 $\Omega \cdot$ m basin sediments had no lateral bounds, i.e., formed a continuous layer. Both ρ_{xy} and ρ_{yx} for the 3-D body fall increasingly below the 1-D sounding as frequency falls, while both ϕ_{xy} and ϕ_{yx} generally exceed the 1-D response at lower frequencies. For point A, ρ_{xy} and ϕ_{xy} are less anomalous than ρ_{yx} and ϕ_{yx}, because the resistivity boundaries normal to the incident electric field in the former case are more distant relative to their dimensions. Still, all the 3-D signatures depart substantially from the 1-D response. As explained with the pseudosections, free charges on the boundaries of the 3-D model cause a progressive depression of the electric fields for both modes over the basin as frequency decreases.

Also in Figure 18, the 3-D responses are compared to results over the 2-D model of identical cross-section. The 2-D TE response is quite similar to the 1-D sounding over most of the

frequency range, but it shows some departure toward lower frequencies. Due to the boundary charges, the difference between the 2-D TE and corresponding 3-D responses is much more striking. On the other hand, the 2-D TM results compare well with ρ_{yx} (3-D) and ϕ_{yx} (3-D) over the whole frequency range, apart from a minor discrepancy mainly in amplitude below about 0.1 Hz. We stress that is difficult to achieve accuracy right over a shallow, high-contrast model since the secondary E-field for which we solve nearly cancels the incident field here. We are especially suspicious of the irregular 3-D behavior around 0.1 Hz. Alternately, a small amount of current gathering in the horizontal plane from the layered host may explain at least partially the difference in these 2-D TM and 3-D results. Nevertheless, very small changes in basin resistivity would result in substantial changes in ρ_{yx} and ϕ_{yx}, either for the 3-D or 2-D bodies, so that in reality these discrepancies are of little consequence.

At point B beside the basin, principal apparent resistivities and impedance phases for the 3-D model are compared in Figure 19 to the response of the 1-D regional resistivity profile in the absence of the basin. The 3-D response in ρ_{xy} falls increasingly below the response of the regional host ρ_ℓ for frequencies below about 10 Hz while that in ϕ_{xy} exceeds ϕ_ℓ,
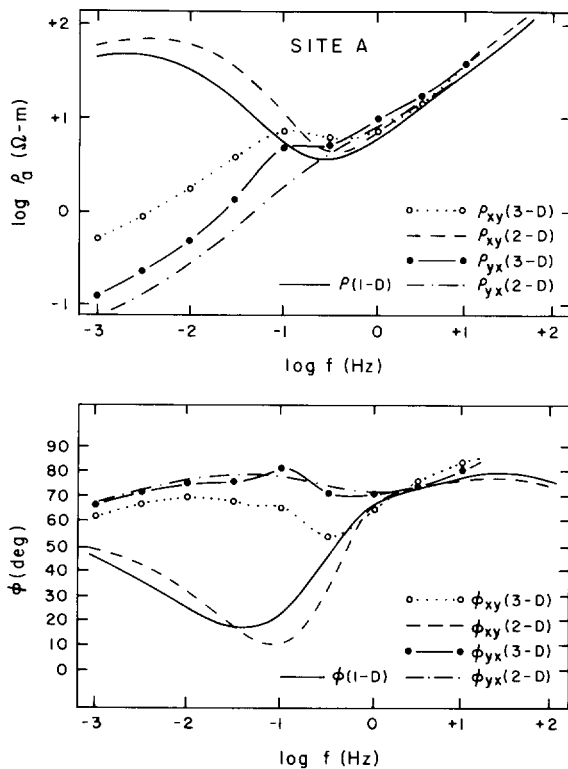
FIG. 18. Principal apparent resistivities and impedance phases ρ_{xy} and ϕ_{xy} (dotted curves, identified as TE) and ρ_{yx} and ϕ_{yx} (dashed curves, identified as TM), for point A over the basin model of Figure 8. The 3-D responses were calculated every half decade in frequency, as shown by the open and solid circles. For comparison, the 1-D response which would occur if the basin had no lateral bounds is shown with solid curves. Also presented are the results for a 2-D basin model of identical cross-section.
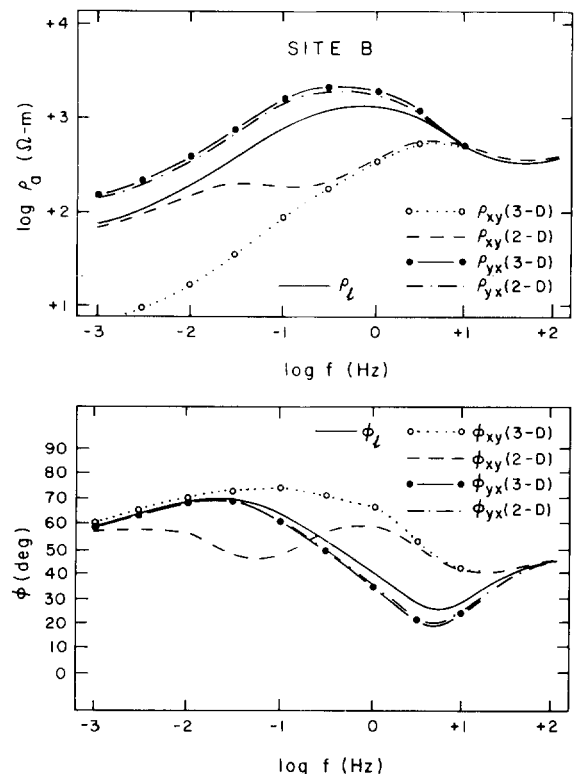
FIG. 19. Principal apparent resistivities and impedance phases for point B over the basin model of Figure 8. Plotting convention is the same as that in Figure 16. For comparison, the 1-D response of the regional host to the basin model shown in Figure 8 is plotted with solid curves. Also presented are the results for a 2-D basin model of identical cross-section.

especially over the middle frequency range. On the other hand, the 3-D response ρ_{yx} increases beyond ρ_ℓ while ϕ_{yx} is less than ϕ_ℓ, again especially at mid-frequencies. For point B, ρ_{yx} and ϕ_{yx} are less anomalous than ρ_{xy} and ϕ_{xy} for the 3-D body. As explained also with the pseudosections, free charges on the ends of the 3-D basin model depress electric fields both over and adjacent to the basin model for the TE mode. However, charges on the sides of the model result in an undershoot-to-overshoot behavior in the electric field causing depression of ρ_{yx} over the basin but amplification of ρ_{yx} to the side with respect to ρ_ℓ. These 3-D results are similar to those presented by Park et al. (1983).

The 3-D results at site B have been compared as well to those beside the 2-D model. The 2-D TE response here differs a great deal from ρ_ℓ and ϕ_ℓ, showing an apparent resistivity minimum near 0.2 Hz along with a maximum in ϕ_{xy} (2-D) at somewhat higher frequencies. Unlike the 3-D values which decrease monotonically, the 2-D TE apparent resistivities approach the layered host sounding at low frequencies. Again, however, the 2-D TM signatures very much resemble the corresponding 3-D calculations over the entire frequency range. We are not certain how much of the apparent difference is due to numerical inaccuracy and how much is 3-D current gathering, but the difference is very small anyway.

Principal apparent resistivities and impedance phases shown in Figures 20 and 21 for sites C and D outside the 3-D basin model qualitatively are similar to those at site B. However, in contrast to responses at B, ρ_{yx} and ϕ_{yx} at C and D appear essentially as anomalous as ρ_{xy} and ϕ_{xy} when compared to the regional profile sounding. For site D in particular, current gathers from large volumes of the host toward the corner of the basin model resulting in large electric fields and large values of ρ_{yx}. Furthermore, an apparent resistivity anisotropy exceeding two orders of magnitude has occurred here.

Note especially that the transverse electric apparent resistivity defined in the conventional manner is depressed relative to the response of the 1-D host alone everywhere over and exterior to the conductive 3-D body to arbitrarily low frequencies. In light of the concept of EM scaling, such depression can be as severe locally about small conductive bodies as about large ones. Given this depression, we are skeptical of many published models of layered resistivity structure in the Basin and Range and other extensional regimes. We believe many such models have erroneously shallow depths to interfaces and erroneously low values of layer resistivities (see also Porath, 1971a; Wannamaker, 1983).

To be sure, our skepticism is based upon the assumption that upper crustal lateral inhomogeneities, for the greater part, are conductive compared to their environs. It has been argued previously that this is the case for sedimentary distributions.
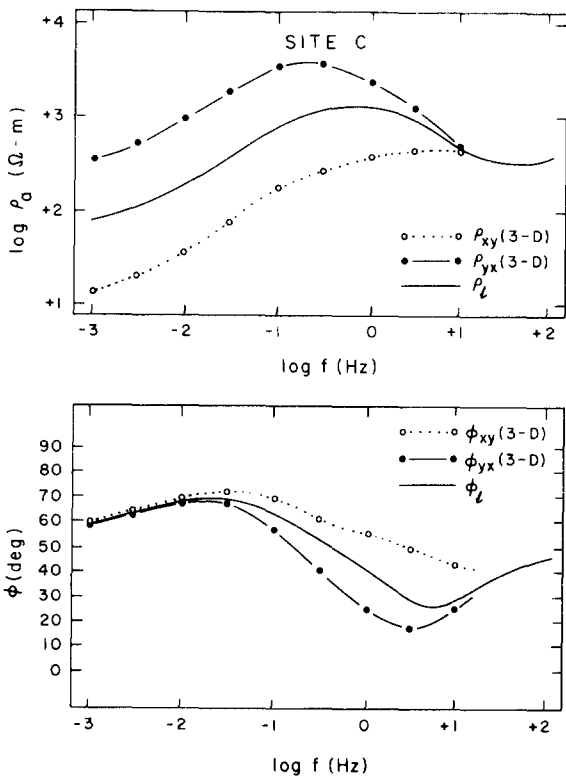
FIG. 20. Principal apparent resistivities and impedance phases for point C of the end of the basin model of Figure 8 compared to the 1-D response of the regional host. Plotting convention is the same as that in Figure 18.
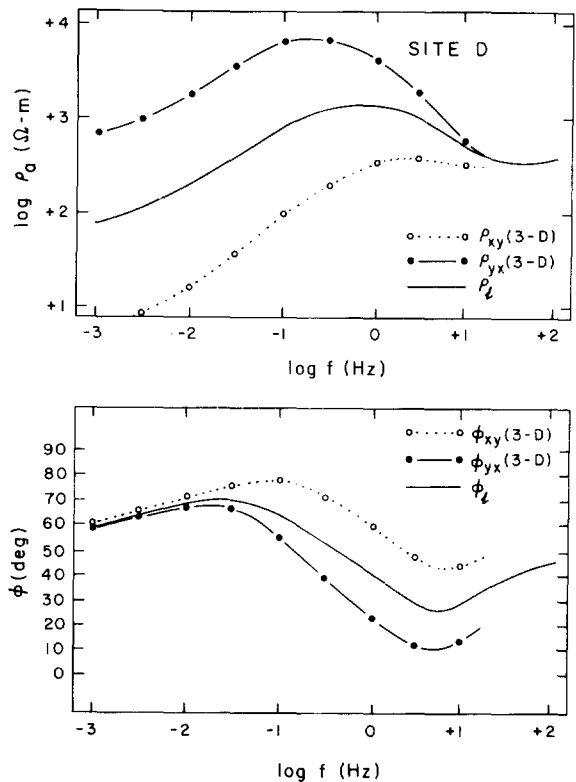
FIG. 21. Principal apparent resistivities and impedance phases for point D outside the corner of the basin model of Figure 8 compared to the 1-D response of the regional host. Plotting convention is the same as that in Figure 18.

However, even if resistive inhomogeneities were as common as conductive ones, our perception of a bias toward low resistivity at depth probably still is valid. This bias occurs because, for a given body-host layer resistivity contrast, the upward shift in the TE apparent resistivity about a resistive body is less than the downward shift in this function about a conductive body (Berdichevskiy and Dmitriev, 1976).

CONCLUSIONS

Resistivity structure in nature is an ensemble of inhomogeneities of different scales, and the small structures in this collection may have MT responses as strong as those of the large ones. Any telluric distortion in overlying, small-scale extraneous structure will be superimposed upon the apparent resistivities measured over buried 3-D targets to arbitrarily low frequencies. However, the responses of the small and large bodies have frequency dependencies that are separated approximately as the square of the geometric scale factor distinguishing the different structures. Also, the magnitudes of the tipper elements as well as the phases of all MT functions due to a particular body are significant only over a finite frequency range, i.e., they are band-limited. Thus, these quantities may allow one to "see through" small-scale extraneous structure to observe the signature of a buried target if the scales of the two types of inhomogeneity differ sufficiently.

Relative to the TE response of a 2-D body of identical cross-section, the apparent resistivity identified as TE by conventional means over and around a confined 3-D conductive body suffers a widespread depression that is increasingly pronounced toward lower frequencies. This depression of the 3-D response results from current gathering. Interpretation of such a 3-D response using 1-D or 2-D TE modeling routines would infer erroneously low resistivities at depth below the true inhomogeneity. From this we conclude that many published models of deep resistivity derived from MT have experienced a bias toward shallow, low resistivities.

Fortunately, our model studies have shown that centrally located profiles of apparent resistivity ρ_{yx} and impedance phase ϕ_{yx} across elongate, geometrically regular 3-D prisms can be modeled accurately with a 2-D TM algorithm. Boundary charges are included in both 3-D and 2-D TM formulations. To define pseudosections for transverse magnetic modeling, we recommend employment of a fixed coordinate system based on tipper-strike. Since $[\tilde{\mathbf{K}}_z(\mathbf{r})]$ is band-limited, one may choose an optimal frequency for defining a tipper-strike to minimize the contributions of secondary structures much smaller or, for that matter, much larger than the target.

ACKNOWLEDGMENTS

REFERENCES

Berdichevskiy, M. N., and Dmitriev, V. I., 1976, Basic principles of interpretation of magnetotelluric curves, *in* Geoelectric and geothermal studies: A. Adam, Ed., Akademini Kiado, 165–221.

Boehl, J. E., Bostick, F. X., Jr., and Smith, H. W., 1977, An application of the Hilbert transform to the magnetotelluric method: Elec. Geophys. Res. Lab. Rep., Univ. of Texas at Austin, 98 p.

Brace, W. F., 1971, Resistivity of saturated crustal rocks to 40 km based on laboratory measurements, *in* The Structure and Physical Properties of the Earth's crust: J. G. Heacock, Ed., AGU Mono. 14, 243–256.

Cagniard, L., 1953, Basic theory of the magnetotelluric method of geophysical prospecting: Geophysics, **18**, 605–635.

Cook, K. L., Adhidjaja, J. I., and Gabbert, S. C., 1981, Complete Bouguer gravity anomaly and generalized geology map of Richfield 1° × 2° quadrangle, Utah: Map 59, Utah Geological and Mineral Survey, Salt Lake City.

Eaton, G. P., 1982, The Basin and Range province: origin and tectonic significance: Ann. Rev. Earth Plan. Sci., **10**, 409–440.

Erwin, J. W., and Berg, J. C., 1977, Bouguer gravity map of Nevada-Reno sheet: Map 58, Nevada Bureau of Mines and Geology.

Erwin, J. W., and Bittleston, J. C., 1977, Bouguer gravity map of Nevada-Millett sheet: Map 53, Nevada Bureau of Mines and Geology, Reno.

Gamble, T. D., Goubau, W. M., and Clarke, J., 1979, Magnetotellurics with a remote reference: Geophysics, **44**, 53–68.

Gamble, T. D., Goubau, W. M., Goldstein, N. E., Miracky, R., Stark, M., and Clarke, J., 1981, Magnetotelluric studies at Cerro Prieto: Geothermics, **10**, 169–182.

Gamble, T. D., Goubau, W. M., Miracky, R., and Clarke, J., 1982, Magnetotelluric regional strike: Geophysics, **47**, 932–937.

Grant, F. S., and West, G. F., 1965, Interpretation theory in applied geophysics: McGraw-Hill Book Co., Inc., 584 p.

Harrington, R. F., 1961, Time-harmonic electromagnetic fields: McGraw-Hill Electrical and Electronic Engineering Series, McGraw-Hill Book Co., Inc., 480 p.

Healey, D. L., Snyder, D. B., and Wahl, R. R., 1981, Bouguer gravity map of Nevada-Tonopah Sheet: Map 73, Nevada Bureau of Mines and Geology.

Hermance, J. F., 1982, The asymptotic response of three-dimensional basin offsets to magnetotelluric fields at long periods: The effects of current-channeling: Geophysics, **47**, 1562–1573.

Hermance, J. F., and Thayer, R. E., 1975, The telluric-magnetotelluric method: Geophysics, **40**, 664–668.

Hintze, L. F., 1980, Geologic map of Utah: Utah Geological and Mineral Survey, Salt Lake City, Utah.

Jones, F. W., and Vozoff, K., 1978, The calculation of magnetotelluric quantities for three-dimensional conductivity inhomogeneities: Geophysics, **43**, 1167–1175.

Klein, D. P., and Larsen, J. C., 1978, Magnetic induction fields (2-30 cpd) on Hawaii Island and their implications regarding electrical conductivity in the oceanic mantle: Geophys. J. Roy. Astr. Soc., **53**, 61–77.

Kunetz, G., 1972, Processing and interpretation of magnetotelluric soundings: Geophysics, **37**, 1005–1021.

Larsen, J. C., 1975, Low frequency (0.1-6.0 cpd) electromagnetic study of the deep mantle electrical conductivity beneath the Hawaiian Islands: Geophys. J. Roy. Astr. Soc., **43**, 17–46.

—— 1977, Removal of local surface conductivity effects from low frequency mantle response curves: Acta Geod. Geop. et Mont. Acad. Sci., **12**, 183–186.

—— 1981, A new technique for layered earth magnetotelluric inversion: Geophysics, **46**, 1247–1257.

Park, S. K., Orange, A. S., and Madden, T. R., 1983, Effects of three-dimensional structure on magnetotelluric sounding curves: Geophysics, **48**, 1402–1405.

Petrick, W. R., Pelton, W. H., and Ward, S. H., 1977, Ridge regression inversion applied to crustal resistivity sounding data from South Africa: Geophysics, **42**, 995–1005.

Porath, H., 1971a, A review of the evidence on low-resistivity layers in the earth's crust, *in* The structure and physical properties of the Earth's crust: J. G. Heacock, Ed., AGU Mono. **14**, 127–144.

—— 1971b, Magnetic variation anomalies and seismic low-velocity zone in the western United States: J. Geophys. Res., **76**, 2643–2648.

Price, A. T., 1973, The theory of geomagnetic induction: Phys. of the Earth and Plan. Int., **7**, 227–233.

Ranganayaki, R. P., and Madden, T. R., 1980, Generalized thin sheet analysis in magnetotellurics: an extension of Price's analysis: Geophys. J. Roy. Astr. Soc., **60**, 445–457.

Rijo, L., 1977, Modeling of electric and electromagnetic data: Ph.D. thesis, Univ. of Utah.

Rooney, D., and Hutton, V. R. S., 1977, A magnetotelluric and magneto-variational study of the Gregory Rift Valley, Kenya: Geophys. J. Roy. Astr. Soc., 51, 91–119.

Sandberg, S. K., and Hohmann, G. W., 1982, Controlled-source audio-magnetotellurics in geothermal exploration: Geophysics, 47, 100–116.

Stanley, W. D., Boehl, J. E., Bostick, F. X., Jr., and Smith, H. W., 1977, Geothermal significance of magnetotelluric soundings in the Snake River Plain—Yellowstone region: J. Geophys. Res., 82, 2501–2514.

Stewart, J. H., 1980, Geology of Nevada: Nevada Bureau of Mines and Geology Special Pub. 4, 136 p.

Stodt, J. A., 1978, Documentation of a finite element program for solution of geophysical problems governed by the inhomogeneous 2D scalar Helmholtz equation: NSF Program Listing and Documentation, Univ. of Utah, 66 p.

——— 1983, Noise analysis for conventional and remote reference magnetotellurics: Ph.D. thesis, Univ. of Utah, 220 p.

Stodt, J. A., Hohmann, G. W., and Ting, S. C., 1981, The telluric-magnetotelluric method in two- and three-dimensional environments: Geophysics, 46, 1137–1147.

Stratton, J. A., 1941, Electromagnetic theory: McGraw-Hill International Series in Pure and Applied Physics, McGraw-Hill Book Co., Inc., 615 p.

Swift, C. M., 1967, A magnetotelluric investigation of an electrical conductivity anomaly in the southwestern United States: Ph.D. thesis, Massachusetts Institute of Technology, 211 p.

Ting, S. C., and Hohmann, G. W., 1981, Integral equation modeling of three-dimensional magnetotelluric response: Geophysics, 46, 182–197.

Vozoff, K., 1972, The magnetotelluric method in the exploration of sedimentary basins: Geophysics, 37, 98–141.

Wannamaker, P. E., 1983, Resistivity structure of the Northern Basin and Range, in The role of heat in the development of energy and mineral resources in the Northern Basin and Range Province: Geothermal Resources Council, Special Rep., 13, 345–362.

Wannamaker, P. E., Sill, W. R., and Ward, S. H., 1978, Magnetotelluric observations at the Roosevelt Hot Springs KGRA and Mineral Mts., Utah: Geothermal Resources Council Trans., 2, 697–700.

Wannamaker, P. E., Hohmann, G. W., and San Filipo, W. A., 1984, Electromagnetic modeling of three-dimensional bodies in layered earths using integral equations: Geophysics, 49, 60–74.

Ward, S. H., 1967, Electromagnetic theory for geophysical application, in Mining geophysics, v. II: Soc. Expl. Geophys.

Ward, S. H., Parry, W. T., Nash, W. P., Sill, W. R., Cook, K. L., Smith, R. B., Chapman, D. S., Brown, F. H., Whelan, J. A., and Bowman, J. R., 1978, A summary of the geology, geochemistry and geophysics of the Roosevelt Hot Springs thermal area, Utah: Geophysics, 43, 1515–1542.

Weinstock, H., and Overton, W. C., Jr., Eds., 1981, SQUID applications in geophysics: Soc. Expl. Geophys., 208 p.

Word, D. R., Smith, H. W., and Bostick, F. X., Jr., 1970, An investigation of the magnetotelluric tensor impedance method: Elec. Geophys. Res. Lab. Report 82, Elec. Res. center, Univ. of Texas at Austin, 264 p.

——— 1971, Crustal investigations by the magnetotelluric impedance method, in The structure and physical properties of the Earth's crust: J. G. Heacock, Ed., AGU Mono. 14, 145–167.